ELECTROCHEMICAL AND INFRARED STUDIES OF THE ELECTROSORPTION OF 4-METHOXYPYRIDINE ON CRYSTALLOGRAPHIC SURFACES OF GOLD

A Thesis Submitted to the College of Graduate Studies and Research

In Partial Fulfilment of the Requirements for the Degree of

Master of Science

In the Department of Chemistry

University of Saskatchewan

Saskatoon, Canada

By

BIPINLAL UNNI

February 2016

PERMISSION TO USE

In presenting this thesis in partial fulfilment of the requirements for a Postgraduate degree from the University of Saskatchewan, I agree that the Libraries of this University may make it freely available for inspection. I further agree that permission for copying of this thesis in any manner, in whole or in part, for scholarly purposes may be granted by the professor who supervised my thesis work or, in his absence, by the Head of the Department or the Dean of the College in which my thesis work was done. It is understood that any copying or publication or use of this thesis or parts thereof for financial gain shall not be allowed without my written permission. It is also understood that due recognition shall be given to me and to the University of Saskatchewan in any scholarly use which may be made of any material in my thesis.

Requests for permission to copy or to make other use of material in this thesis in whole or part should be addressed to:

Head of the Department of Chemistry
University of Saskatchewan
Saskatoon, Saskatchewan (S7N 5C9)
Canada

ABSTRACT

A firm knowledge about the interaction between the metal surface and adsorbed molecules is imperative for formulating procedures to synthesize nanoparticles (NPs) with predetermined shape and size. The ligand-metal interaction during NP formation can be mimicked on an electrode surface by electrosorbing ligand molecules on a charged metal surface. Electrochemical methods can provide an ideal platform to study the adsorption behaviour of molecules at the solid-liquid interface. In addition to classical electrochemical techniques, the combination of spectroscopy with electrochemical methods amplifies mechanistic insights about the surface adsorption processes. The adsorption behaviour of pyridine and one of its derivatives, 4-dimethylamino pyridine (DMAP) have been well studied due to their potential application in nanoparticle synthesis. However, prior to this work, there has been very limited and conflicting literature available about the adsorption of of pyridine derivatives analogous to DMAP. Among the pyridine derivatives that were studied, some reports indicate that, other than DMAP, only 4-methoxy pyridine (MOP) can stabilize gold nanoparticles. However, very little is known about the possible differences in the adsorption energy and general behaviour of MOP compared to DMAP. Resolving this knowledge gap is imperative to resolving the conflicting information about pyridine-based stabilizers for metal nanoparticle applications.

The adsorption behaviour of MOP on different crystallographic Au surfaces as a function of pH and surface potential has been investigated in this project. These studied were carried out using classical electrochemical methods including chronocoulometry and differential capacity, as well as modern spectroscopic techniques like Surface Enhanced Infrared Absorption Spectroscopy (SEIRAS). The thermodynamic parameters obtained from electrochemical data shows that adsorption features of MOP is similar to that of DMAP.

However, there is a significant difference in the adsorption strength of MOP and DMAP at positive potentials. The SEIRAS data provides much more detailed information about the potential depended orientation of MOP on polycrystalline Au. Cumulative analysis of electrochemical and spectroscopic data provides strong evidence that MOP can stabilize Au(111) facets over wide pH ranges. Moreover, this work provides convincing evidence that the basic nature of substituted pyridine alters the metal to ligand adsorption strength.

ACKNOWLEDGEMENT

I express my gratitude to Dr. Ian J. Burgess for his guidance and support throughout this research. Also, my sincere thanks to my graduate advisory committee members Dr. Robert Scott and Dr. Ike N. Oguocha for their valuable comments on my research and thesis.

I acknowledge the Department of Chemistry, University of Saskatchewan for the financial support during the course. My special thanks to the lab manager Dr. Alexandra B. Scott.

I extended my heartfelt thanks to Burgess Group for their encouragement and cooperation for the successful completion of this research work. And finally, a big thanks to my family and friends for being with me.

TABLE OF CONTENTS

Chapter 5

LIST OF FIGURES AND TABLES

LIST OF SYMBOLS AND ABBREVIATIONS

DMAP	4-Dimethylamino pyridine
MOP	4-Methoxypyridine
$MOPH^+$	4-Methoxypyridinium
MOP/H^+	4-Methoxypyridine and/or 4-Methoxypyridinium
NP	Nanoparticle
LSPR	Localized Surface Plasmon Resonance
IR	Infrared
TOAB	Tetraoctylammonium bromide
ODA	Octadecyl amine
SEIRAS	Surface Enhanced Infrared Absorption Spectroscopy
DC	Differential Capacity
$\mathcal{E}_0$	Permittivity of free space
$\mathcal{E}_r$	Relative permittivity
K_a	Acid dissociation constant
pzc	Potential of zero charge
σ_m	Charge density on metal surface
E	Electrode potential
Γ	Gibbs surface excess
ac	Alternating current
dc	Direct current
Re	Real component
Q	Imaginary component
ω	Angular frequency
CC	Chronocoulometry

C	Coulomb
V	Volt
μ	Micro
F	Farad
M	Molar
E_{base}	Base potential
E_{var}	Variable potential
E_{des}	Desorption potential
Π	Surface pressure
χ	Mole fraction
Γ	Surface tension
R	Molar gas constant
G	Activity coefficient
M	Chemical potential
T	Temperature
K_{ads}	Adsorption rate constant
ΔG^0_{ads}	Standard free energy of adsorption
ATR	Attenuated Total Reflection
ocp	Open circuit potential
Abs	Absorbance
R_E	Spectra at E potential
R_{Eref}	Spectra at reference potential
TDM	Transition dipole moment
A′	Vibration along molecular plane
A′′	Vibration orthogonal to molecular plane

δ	Bending mode
υ	Stretching mode
UHV	Ultra high vacuum

Chapter 1

Background and literature review

1.1 **Why Does "Nanomatter" Matter?**

When the spatial dimensions of a discrete piece of macro-sized material are scaled down to nanometer size, the behaviour of the electrons within that material and their interaction with the lattice nuclei can undergo a fundamental change. For example, for nanosized metals, electrons get confined by the lattice and the average electronic energy level spacing (Kubo gap[1]) increases. The change in the Kubo gap alters the electronic, optical and magnetic properties of the material at nanoscale dimensions.[2] On the other hand, sometimes scaling down the size of the material is beneficial for simple geometric reasons, an example being the dramatic increase in the percentage of surface atoms with respect to volume offered by metal nanoparticles.[3] Thus, the material properties of a nanosized object are often fundamentally different from those of the same matter in macroscale form. Quite simply, "nanomatter" matters because of the potential applications of its fundamental properties. Critically because the properties of nanomaterials are tunable with respect to their size and shape, nanotechnology opens a vast possibility of development in many aspects of science and technology. Although materials at the nano level exhibit a host of attractive properties and even broader applications, a comprehensive discussion of nanomaterial properties and applications is beyond the scope of this Chapter. Instead, the discussion will focus on metal nanoparticles (NPs). Noble metal nanoparticles are prominent in the advancement of science and technology and have appealing properties for fields ranging from catalysis, photonics, electronics, energy storage and medicine.[4,5,6,7]

1.2 **Applications of Metal NPs**

One of the attracting optical properties of Au and Ag NPs is the localized surface plasmon resonance (LSPR), which is due to the collective oscillation of free electrons at the metal surface, coherent with the oscillating electric field of incident light.[8] The size and shape of the nanocrystal* determine the electronic polarisation and charge distribution on the metal surface due to resonance of a localized surface plasmon. Hence, all LSPR phenomena such as the number of resonance peaks, their frequency, and the ratio between scattering and absorption cross section are determined by the NP size and its aspect ratio. For example, aqueous dispersions of 50 nm diameter Au nanospheres shows a strong absorption peak at ca. 525 nm, whereas Au nanorods with an aspect ratio of 5:1 shows two LSPR peaks. The peak at ~540 nm is attributed to electronic oscillations along short axis and another at ~825 nm due to the electronic oscillations along the long axis.[9,10] Hence, fine tuning of LSPR is possible by fabricating NPs with desired shape and size. For application purposes the wavelength of the LSPR matters because the strong localized electromagnetic fields that arise in the vicinity of the NP upon excitation of the plasmon can enhance the Raman and IR signals of the molecules, adsorbed onto or nearby the metal NP surfaces, by many orders of magnitude. This phenomenon is the basis of various surface-enhanced spectroscopic techniques.[11,12,13] Due to the enhancement effect, surface-enhanced spectroscopic techniques can be used to detect molecules of ultra low concentrations (10^{-15} moles).[14] Apart from surface-enhanced spectroscopies, light scattering phenomena as a result of LSPR of NPs is utilized in optical imaging techniques such as optical coherence tomography (OCT) and dark-field microscopy. In OCT, enhanced image contrast is made possible by the presence of NPs with large

* The term 'nanocrystal' will often be used in this thesis as a synonym for NP to emphasize the crystalline nature of the nanostructures.

scattering cross section. In dark-field microscopy, the scattered light from the particle is collected to obtain particles with bright colours against a dark background. The photothermal effect is yet another phenomenon which can arise from plasmonic excitation of metal nanoparticles. Non-radiative energy loss acts as a localised heat source in nano or micro confinements upon irradiating NPs with a suitably tuned laser. Photoacoustic imaging can also be achieved by capitalizing on the localized heating described above. The coupling of plasmons from NPs due to agglomeration results in dramatic color changes of the NP suspension. Hence, colorimetric sensors are another application resultant from the sensitivity of LSPR towards the dielectric nature and agglomeration of metal NPs.[15]

As well as the optical properties described in the preceding paragraph, metal nanoparticles also offer particular advantages for catalysis. The scope of NP in catalysis has been extensively explored. Although the large surface area available for reaction is the primary attraction of NPs as catalysts, the chemical activity, specificity and selectivity of nanocatalysts can be tuned by controlling its morphology. For example, the product of benzene hydrogenation catalyzed by 13 nm sized Pt cuboctahedrons, with both {111} and {100} facets, are cyclohexane and cyclohexene. However, the same reaction catalysed by same sized Pt NPs of cubic geometry with almost exclusively {100} facets produces only cyclohexene.[16] Another example is the observation that 6 nm Pd nanocubes with {100} facets show one order magnitude higher oxygen reduction activity than their counterparts with {111} facets.[17]

1.3 **Synthesising Anisotropic NPs**

The examples in section 1.2 illustrate the need to make NPs with desired shape and surface crystallography. Meanwhile, synthesis of anisotropic metallic NPs with good reproducibility is a bottleneck to widen its applications. One of the earlier strategies to make

colloidal metal nanocrystals in solution was through a one-pot synthesis.[18] This method involves nucleation from metallic atoms/ions followed by seed formation. Eventually, these seeds will evolve into nanocrystals. However, this method lacks control over the final size and shape of the NP. Fortunately, the last decade has witnessed a significant effort by the scientific community in developing methods for shape and size selective NP synthesis. The real breakthrough in making anisotropic noble metal NPs was the 'seed-mediated' synthesis[19] reported by Jana and Murphy in 2002 who reported a means to produce gold nanorods. Subsequently, the seed-mediated growth process was refined by many other groups (El-Sayed *et al.*, Gai *et al.*)[20]. Seed-mediated synthesis involves three steps i) synthesis of seeds with defined crystal structure, ii) addition of growth solution (containing the metal precursor, growth directing agents and mild reducing agents) to the seed solution and iii) the reduction of metal ions by mild reducing agents that are catalyzed by the seed particle. Thus, the newly reduced metal atoms get deposited onto the seed surface without further nucleation.

The initial hypothesis about the nanorod growth mechanism proposed by Murphy *et al*. was that the formation of gold nanorods was due to the diffusion of metal atoms into the soft templates formed by the orderly arrangement of surfactant micelles. In their later reports,[9, 21] the authors excluded their initial hypothesis about growth mechanism and proposed that the site-specific adsorption of surfactants could result in the growth of anisotropic NPs. Gai *et al.*[20b] suggested a similar growth mechanism regarding the formation of Au nanorods. According to these authors, multiply twinned seeds offer lower surface energy compared to single crystal seeds. Nanorod growth happens by the diffusion of Au atoms to the twinned areas where surfactants are weakly bound. They also claimed to be the first to provide direct evidence for the stabilization of high energy surfaces by surfactants. El-Sayed *et al.*[22] reported another study about the synthesis of Au nanorods in which they outlined the role of site-

specific adsorbed surfactants in breaking the symmetry of the seed to evolve into stable anisotropic nanostructures. El-Sayed's group reported a better approach in synthesizing large densities of high aspect ratio Au nanorods with uniform length by introducing multiple capping agents into the reaction mixture.

If the rate at which newly reduced atoms are produced near the seed crystal is low enough such that surface diffusion is faster than the rate of deposition, then the crystal will grow to produce the most thermodynamically stable construct.[23] Typically, this means the nanocrystal shows proportional growth along its unit cell dimensions to obtain a shape with minimum surface energy. The growth of the nanocrystal into different geometries from its symmetric unit cell dimension requires an extrinsic force. Altering the reaction conditions can break the symmetry during the growth process. One of the strategies to induce asymmetric nanocrystal growth on seeds, with well-defined crystal faces, is to introduce capping agents to the growth solution. Capping agents are usually ionic species, small molecules or even macromolecules that can bind selectively to specific crystals facets to reduce surface energy. The extent of reduction in surface energy depends upon the surface density of capping agent. Capping agents strongly adsorbed to particular facets passivate the surface for the deposition of newly formed atoms from growth solution. Also, the chemisorption of the capping agent will increase the energy barrier to surface diffusion causing differential growth rates of the nanocrystal[24] and the generation of particle anisotropy. The prediction of the growth process of single crystal seeds in the presence of capping agent described by Xia[23] in one of his recent perspectives is summarized below. Upon introducing a capping agent with preferential adsorption on {100} facets into truncated octahedral seed solution, there will be a shift in the surface energy of facets; $\gamma_{\{100\}} < \gamma_{\{111\}}$. This will result in faster growth in the <111> direction than in the <100> direction, thus the ratio of {100} to {111} facet areas on the surface will

increase. The truncated octahedron will evolve into a cuboctahedron, truncated cube and finally a cube enclosed by {100} facets only. Conversely, in the presence of capping agent for {111} facets, truncated octahedron seeds will grow and evolve into octahedra with only {111} facets at the surface. Even though a rich variety of capping agents for controlling shape and size of NP can be identified in the current literature, there exists a lacuna in understanding the working mechanism of capping agents. Often, only after the generation of favourable anisotropic nanocrystals, the concept of preferential capping agent adsorption on particular facets is deduced. Due to the lack of quantitative experimental data, the theoretical and computational approach in understanding structure directed growth of NPs suffers from poor accuracy.[25] Fundamental studies of capping agent adsorption are needed to alleviate this problem and provide the motivation for this thesis.

1.4 **Capping Agents and Phase Transfer**

Apart from directing NP growth, capping agents play many other important roles in nanoparticle chemistry. Due to high surface area-to-volume ratio, NPs are thermodynamically unstable structures. Hence, NPs synthesised in solution phase show an inherent tendency to agglomerate. The presence of capping agents at the NP surface prevents them from fusing together. The capping agents also dictate which media the NPs can remain freely dispersed. Relatively non-polar capping agents will lead to dispersions in organic solvents whereas the presence of charged or strongly polar molecules on the metal surface will allow dispersion in water. It is often desirable to move NPs from the original medium of synthesis to a different medium. For strongly bound capping agents such as alkanethiols, nanocrystals can be isolated from the solvent and then re-suspended. However, this is not the case for weaker bound surfactants, and phase-transfer methods must be employed.[26]

The Brust-Schiffrin[27] method is one of the well-established procedures to prepare organic soluble Au NPs. In this approach, the metal precursor is extracted from the aqueous phase to the organic phase (toluene) using tetraoctylammonium bromide (TOAB) which acts as a phase transfer agent. Subsequently, the metal ions in the organic phase are reduced with $NaBH_4$ in aqueous solution in the presence of alkanethiols (capping agent). There have been extensive efforts to modify the Brust-Schiffrin method to tune the NP size and dispersion by varying the alkyl thiol chain length, using aromatic rather than aliphatic thiols, and adjusting precursor-to-thiol ratio.[28,29,30] Beyond the high stability of thiol-Au NPs due to the strong Au-S bond (~ 47 kcal/mol)[31], thiol ligands constrict the NPs for post-synthesis surface modification. Thus, thiol-stabilized Au NPs have less utility for applications such as biosensors and optics. An alternative to overcome the drawbacks of thiol ligands is to use labile ligands like amines. In the seminal work on self-assembled amine monolayers on Au, Crooks *et al.*[32] showed the formation of good quality monolayers of $CH_3(CH_2)_9NH_2$ through vapour deposition on bare Au substrates. Meanwhile, Leff *et al.*[33] successfully modified the Brust-Schiffrin method by using alkyl amines. Even with these modifications, the Brust-Schiffrin method still showed many drawbacks such as impurities in the final products from the phase transfer agents, incomplete phase transfer due to the poor interaction of capping agents (irrespective of thiols and amines) to the phase transfer agents, and incompatibility between the capping agents and the reducing agent.[26]

While the above example illustrates the use of surfactants to act as water-to-organic phase transfer agents, it is often desirable to perform the opposite operation as water compatibility is an essential prerequisite for the application of NPs in biological or environmental systems. Although numerous protocols are now available for water soluble NP synthesis, the agglomeration tendency of NPs in polar media leads to activity loss. A common approach is

water soluble NP synthesis at low concentration[34] (~ 5 x 10^{-4} M) at the cost of high throughput; which is a limitation towards biological sensing and imaging applications. In contrast, relatively high concentrations of NPs (up to 1 M) with controlled size and shape can be obtained from non-polar solvent based NP synthesis.[35,36,37] Phase transferring the Au NPs synthesised in organic solvents to aqueous phase can provide NPs bestowed with high density, monodispersity and water compatibility. Unfortunately, there are not many reports about reverse phase transfer available in any of the current literature. Schmid *et al.*[38] made a pioneering attempt in reverse phase transfer to synthesize phosphorus stabilized Au_{55} clusters. Schmid's group prepared $Au_{55}(PPh_3)_{12}Cl_6$ and transferred clusters to water by exchanging the PPh_3 (triphenylphosphine) ligands with $Ph_2PC_6H_4SO_3Na$ (aq). The Au hydrosols were reported to be more stable after phase transfer due to the high ionic charge on the cluster surface. Another report by Simard *et al.*[39] showed reverse phase transfer for the synthesis of water-soluble Au clusters through thiolate ligand exchange. They demonstrated the exchange of alkanethiol-capped Au NPs with ω-thiocarboxylic acid. This process is limited by very long reaction times as the exchange of even half the number of ligands required two days.

In short, despite the greater stability offered by the use of strongly bound capping agents, their irreversible binding to the metal surface is disadvantageous in that it removes the opportunity to exchange the surfactant that removes the possibility of further surface modification. On the other hand, by using labile ligands with functional groups that enable easy and complete ligand exchange, phase transfer of NPs can be facile allowing new opportunities for post-synthetic applications.

Among labile ligands, one of the popular class of ligands is nitrogen-based containing amines (or amino) groups, due to their compatibility with biological and environmental systems. Sastry *et al.*[40] can be credited with the first demonstration of the phase transfer

ability of alkyl amines. They were able to phase transfer Au NPs from aqueous media to toluene using octadecyl amine (ODA). The ODA stabilized Au NPs showed no stability at pH < 5 presumably due to protonation of the tertiary amine although this was not explicitly proven. Nirmala *et al.*[41] have demonstrated the synthesis of Au and Pt NP phase transferred and stabilised using hexadecaaniline. Due to the hydrophobic nature of the tail groups, these ligands are reported for aqueous to organic phase transfer. However, phase transfer seems to occur at a slow pace and only within a narrow range pH stability. Furthermore, some of the synthetic steps are tedious, and post-functionalization is not facile for these ligand stabilized NPs.

1.5 **4-(Dimethylamino)pyridine (DMAP): a Versatile Physisorbed Ligand**

Gittins and Caruso[42] first reported the use of DMAP for phase transferring gold nanoparticles from organic to aqueous media. In their report, DMAP replaces the tetraoctyl ammonium bromide (TOAB) from the surface of Au NPs allowing them to undergo a spontaneous phase transfer from toluene to water. The synthesis procedure of DMAP stabilized Au NPs is very facile and rapid. Moreover, these NPs can phase transfer rapidly from organic to aqueous media where they show no degradation or aggregation for months to years. Somewhat surprisingly DMAP stabilized Au NPs show stability over a wide pH range – a point which will be further addressed below – even though the strength of adsorption is sufficiently low to allow post-fabrication ligand exchange. A report by Rucareanu *et al.*[43] highlight the potential of DMAP as an easily exchangeable ligand. They synthesised Au NPs soluble in both organic media and aqueous media by using DMAP stabilised Au NPs as precursors through ligand exchange reactions. The point to be noted here is, complete ligand replacement happened, and final product contained no residual DMAP unlike alkyl ammonium bromide and alkyl thiol-based synthesis.

In addition to the phase transfer ability, the potential of DMAP stabilized Au NPs has been tapped for versatile applications and some of these interesting reports are mentioned below.

- Gittins and Caruso[44] reported the application of DMAP stabilized Au NPs for biolabeling. They prepared 11-mercaptoundecanoic acid (MUA)–functioned Au NPs through DMAP assisted phase transfer to obtain highly concentrated NP solution, a prime criterion for biological applications. Biver *et al.*[45] studied the interaction of the positively charged outer surface of DMAP -Au NPs with negatively charged DNA strands.
- An increased binding energy of Au orbitals and increased zeta potential values after DMAP stabilization of Au NP attributes to a positively polarized surface of DMAP stabilized AuNPs. Kang *et al.*[46] utilized this surface property of DMAP-Au NPs to fabricate PVP composite membranes to efficiently separate olefin mixtures. This application proves another ability of DMAP-AuNPs as stable olefin carriers for facilitated olefin transport membranes.
- Dong *et al.*[47] prepared DMAP-Au NP-doped polyelectrolyte hollow capsules by making use of the surface polarity and easy ligand exchange nature of DMAP-AuNPs. They were able to obtain a dense layer of Au NPs followed by neat multilayers of polyelectrolytes without any residual DMAP, unlike other ligands. The gold doped polyelectrolyte capsules showed enhanced Raman signals and also were able to study chemical reactions in micro and nanoconfinement.
- Yu *et al.*[48] explored the catalytic activity of DMAP-Au NP systems. Covalently linked ligand molecules adversely affect the catalytic activity of NP. Unlike covalently linked ligands, DMAP can be washed off from the Au NP surfaces, and this feature exposes good catalytic surfaces. Yu *et al.* prepared polyelectrolyte films with densely loaded

DMAP-Au NPs to exploit the catalytic and electronic properties of Au NPs for electrochemical detection of nitric oxide.

1.6 **Fundamental Adsorption Studies**

In a recent perspective, Xia *et al.*[23] provided a detailed description of the thermodynamic and kinetic parameters determining the shape of nanocrystals. According to the author, *'thermodynamic control in a solution phase is a simple and yet effective strategy that can be easily implemented during an experiment'*. Xia suggests the two ways of controlling thermodynamics to manipulate the growth of nanocrystals: *'(i) introducing different types of capping agents that selectively chemisorb onto different types of metal surfaces and thus lowers the specific surface free energies of these facets and (ii) controlling the coverage density of a capping agent by adjusting its concentration in the reaction solution to manipulate its power in lowering the specific surface free energy of a facet'.*

Xia's comments are compelling but what is missing is a strategy to effectively screen the adsorption of capping agents and to determine possible selective adsorption behaviour. Measuring adsorption of labile ligands on nanometer sized surface in the complicated milieu of nanoparticle growth solutions is essentially an intractable problem. The Burgess group has strongly advocated that the required information can be obtained using electrochemical and spectroelectrochemical techniques. Prior to this work, their studies have focused heavily on the DMAP-Au interface, and the results are briefly summarized below.

It was assumed that protonated DMAP cannot stabilize gold NPs because the pyridine-metal interaction was believed to occur through the lone pair of electrons on the endocyclic nitrogen.[49] A resonance structure can be drawn for DMAP with a formal negative charge on the ring nitrogen and a positive charge on the exocyclic nitrogen. Therefore, it was assumed that DMAP binds to the Au through pyridine ring and the positively charged exocyclic

nitrogen at the outer surface enables the phase transfer to the aqueous phase and prevents NP flocculation on the basis of repulsive electrostatic interactions. Gandubert and Lennox[50] supported the pH dependent stability of DMAP-Au system, and they emphasised that excess DMAP is required to stabilize the NP. However, a quantitative measurement of the surface concentration of DMAP, evaluation of the adsorption energy of DMAP on Au, and the molecular orientation of DMAP on Au was entirely missing. Barlow and Burgess[51] addressed these deficiencies by performing differential capacity and chronocoulometry studies to evaluate DMAP adsorption on millimetre-sized polycrystalline Au electrodes. According to their findings, the molecular orientation of DMAP on polycrystalline Au is highly depending on the electrical state of the metal surface as well as the solution pH. The capacitance value of the DMAP film on polycrystalline Au electrode surface at pH ≥ $pK_{a,\ DMAPH+}$ shows that DMAP exclusively binds on polycrystalline Au vertically via its pyridinic nitrogen. However, at acidic pH (<3), DMAP adsorbs on Au *via* π-bonding which results in a horizontal orientation. In these very acidic conditions, DMAP was found to desorb from the Au surface when the electrode surface charge density becomes positive of the potential of zero charge (*pzc*). At moderate electrolyte pHs, the adsorbed DMAP shows a phase transition from horizontal to a vertical orientation when the applied electrode potential shifts from negative to positive values with respect to the pzc. The shift in the molecular orientation results in a threefold increase in the surface density of DMAP on polycrystalline Au. However, the calculated adsorption energy of DMAP at moderate pHs are lower than the DMAP adsorption energy at basic pH (≥ 9.7). These results support the findings of Gittins and Caruso regarding the pH-dependent stability of DMAP stabilized NP but for the first time provide a clear molecular depiction of the capping agent's behaviour.

Vivek and Burgess[52] conducted a detailed study of the crystalline-dependent adsorption of DMAP by comparing the electrosorption behaviour of DMAP on Au (111) and Au (100) with polycrystalline Au surfaces. At high pH conditions, DMAP adsorbs on Au (111) in its basic form and its state of adsorption changes from horizontal with coordination through the pyridine ring to vertical with coordination only through pyridinic nitrogen. The phase transition occurs when the charge density on the electrode surface becomes positive. The authors were able to demonstrate that the phase transition at high pH conditions is specific to the Au (111) surface. Meanwhile, DMAP shows only the high coverage vertical state of adsorption on higher energy Au facets. The adsorption phenomena of DMAP on Au (111) as well as on other crystal faces are again different at acidic conditions (pH ≤ 4.5). Protonated DMAP adsorbs on Au(111) in a horizontal fashion even at positive electrode potentials, whereas $DMAPH^+$ adsorbs horizontally on Au(100) and polycrystalline Au at negative potentials and deprotonates, reorients vertically at far positive potentials. The detailed thermodynamic data of DMAP adsorption on various Au crystal surfaces provided evidence that a high packing density film of DMAP on Au(111) due to its vertical orientation is possible only at high pH and electrode potentials above its *pzc*. Moreover, at pH ≤ 4.5, DMAP adsorption on Au(111) is not favourable even at positive potentials, but a low coverage of $DMAPH^+$ is possible. This information suggests that DMAP cannot stabilize NPs with (111) facets in acidic conditions. Meanwhile, at low pH, there is no evidence for the vertical adsorption of DMAP on Au(100) but DMAP forms high coverage films on polycrystalline electrodes only at positive potentials. This observation indicates that, at low pHs, DMAP forms stable, high-density films only on relatively high energy crystallographic planes. These observations were based on the thermodynamics of ideally polarized electrodes but were confirmed in an independent spectroscopic study by Rosendahl and Burgess.[53] In this work, surface-enhanced infrared absorption spectroscopy (SEIRAS) was used to describe

the adsorption of DMAP on Au as a function of electrolyte pH. This spectroscopic data was in very good agreement with the previous work of Burgess and co-workers although it also revealed additional information on DMAP speciation.

Critically, the fundamental adsorption studies of DMAP demonstrated that DMAP can preferentially adsorb on non-Au{111} facets. The cumulative work predicted a priori that DMAP should act as a capping agent that promotes the formation of anisotropic metal nanoparticles. Fan *et al.*.[54] were subsequently able to manipulate nanoparticle synthesis conditions to promote favourable conditions for the anisotropic growth of Au nanoseeds. The resultant anisotropic nanocrystals (predominantly nanotripods) showed an overgrowth along {111} direction as expected. The success of this approach, namely detailed studies of capping agent adsorption followed by utilization of the results to manipulate anisotropic nanocrystal fabrication, is very appealing. However, it is unclear if the elegance and the approach used in the DMAP system can be extended to other labile capping agents.

1.7 **Motivation and Objectives**

Gittins and Caruso[42] attributed the phenomenal character of DMAP among the pyridine analogues, to stabilize NP, to the *para* substituted tertiary amine (highly basic) conjugated with the electron-donating (weakly basic) group. Lennox *et al.*[50] tested the above hypothesis with 4-aminopyridine, 4-(aminomethyl)pyridine and 4-methoxypyridine. Based on their observations, it was only at very high concentrations that 4-aminopyridine and 4-(aminomethyl) pyridine showed limited phase transfer ability and 4-methoxypyridine (MOP) failed to stabilize NPs.

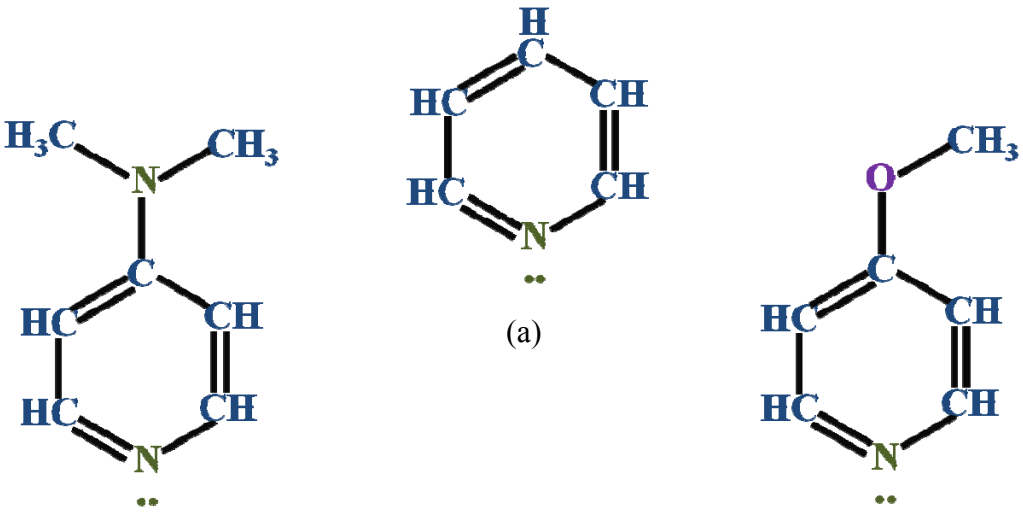

(a) (b) (c)

Figure 1.1. Molecular structure of (a) pyridine (pK_a = 5.25), (b) 4-dimethylaminopyridine (pK_a = 9.70), and (c) 4-methoxypyridine (pK_a = 6.50).

In contradiction to Lennox's report, DFT calculations by Lange *et al.*[55] showed comparable binding energies for both MOP and DMAP on Au. Also, the authors successfully demonstrated phase transfer of Au NPs from toluene to an aqueous phase using MOP, even

though these phase transferred NPs showed moderate agglomeration. Moreover, the calculated binding energy for MOP was higher for the horizontal orientation. Mollenhauer *et al.*[56] also reported a similar theoretical study for the adsorption of pyridine derivatives on Au(111). Their study also shows that the binding energy of pyridine derivatives increases with increasing electron donation ability of the *para* substituent. More importantly, they stated that horizontal adsorption is energetically the most preferred orientation for MOP on Au (111) which seems surprising given the opposite is true for DMAP.

Mollenhauer *et al.*'s research publications are intriguing as generally speaking horizontal adsorption will result in a loosely arranged, less dense capping agent films, but a large density of stabilizing agent on the NP core is imperative to stabilize NP. Therefore, the arguments mentioned in the available literature regarding MOP seem counterintuitive. How can MOP molecules provide sufficient stabilization if they adsorb on Au nanoparticles in a low density orientation? To answer this question, the adsorption of MOP on Au surfaces needs better clarity. Furthermore, by doing so, it is quite conceivable that systematically determining the adsorption behaviour of MOP will open new routes for NP synthesis. Thus the research objectives of this thesis can be concisely defined as follows:

I. Provide an extensive evaluation of 4-methoxypyridine (MOP) adsorption on Au(111) using electrochemical methods.

II. Perform in-situ IR spectroscopic studies of MOP adsorption on Au surfaces to confirm the results of thermodynamic analyses.

III. Provide a comparison of MOP and DMAP adsorption based on their thermodynamic features which can be used to provide commentary on their relative efficacy as nanoparticle stabilizers.

1.8 **Overview of Thesis Structure**

This thesis consists of five chapters. The current chapter has provided a short review of the potential features of anisotropic NPs and scientific efforts in synthesizing shape selective NPs. It also included a brief summary of literature discussing the interesting features of labile ligands, mainly DMAP and its adsorption studies.

The second chapter deals with the experimental methods, instruments, materials used and data analysis methods. Some useful thermodynamic derivations are detailed in this chapter.

Chapter three covers the electrochemical evaluation of MOP on Au(111) using differential capacity and chronocoulometry. The thermodynamic parameters of MOP and DMAP adsorption on Au(111) are also compared here.

Chapter four is about the SEIRAS study of MOP on Au surfaces as a function of pH and potential.

Chapter five discusses the conclusion as well as the relevance of MOP adsorption studies and its scope for future work.

References

1. Kubo, R., Electronic Properties of Metallic Fine Particles. I. *Journal of the Physical Society of Japan* **1962,** *17* (6), 975-986.
2. R Kubo; A Kawabata, a.; Kobayashi, S., Electronic Properties of Small Particles. *Annual Review of Materials Science* **1984,** *14* (1), 49-66.
3. Edwards, P. P.; Johnston, R. L.; Rao, C. N. R., On the Size-Induced Metal-Insulator Transition in Clusters and Small Particles. In *Metal Clusters in Chemistry*, Wiley-VCH Verlag GmbH: 2008; pp 1454-1481.
4. Xia, X.; Tu, J.; Zhang, Y.; Wang, X.; Gu, C.; Zhao, X.-b.; Fan, H. J., High-Quality Metal Oxide Core/Shell Nanowire Arrays on Conductive Substrates for Electrochemical Energy Storage. *ACS Nano* **2012,** *6* (6), 5531-5538.
5. Konstantatos, G.; Sargent, E. H., Nanostructured materials for photon detection. *Nature Nanotechnology* **2010,** *5* (6), 391-400.
6. Haruta, M.; Daté, M., Advances in the catalysis of Au nanoparticles. *Applied Catalysis A: General* **2001,** *222* (1–2), 427-437.
7. Yang, X.; Yang, M.; Pang, B.; Vara, M.; Xia, Y., Gold Nanomaterials at Work in Biomedicine. *Chemical Reviews* **2015,** *115* (19), 10410-10488.
8. Willets, K. A.; Duyne, R. P. V., Localized Surface Plasmon Resonance Spectroscopy and Sensing. *Annual Review of Physical Chemistry* **2007,** *58* (1), 267-297.
9. Murphy, C. J.; Sau, T. K.; Gole, A. M.; Orendorff, C. J.; Gao, J.; Gou, L.; Hunyadi, S. E.; Li, T., Anisotropic Metal Nanoparticles: Synthesis, Assembly, and Optical Applications. *The Journal of Physical Chemistry B* **2005,** *109* (29), 13857-13870.
10. Mulvaney, P., Surface Plasmon Spectroscopy of Nanosized Metal Particles. *Langmuir* **1996,** *12* (3), 788-800.
11. Moskovits, M., Surface-enhanced spectroscopy. *Reviews of Modern Physics* **1985,** *57* (3), 783-826.
12. Hartstein, A.; Kirtley, J. R.; Tsang, J. C., Enhancement of the Infrared Absorption from Molecular Monolayers with Thin Metal Overlayers. *Physical Review Letters* **1980,** *45* (3), 201-204.
13. Fleischmann, M.; Hendra, P. J.; McQuillan, A. J., Raman spectra of pyridine adsorbed at a silver electrode. *Chemical Physics Letters* **1974,** *26* (2), 163-166.
14. Rosendahl, S. M.; Borondics, F.; May, T. E.; Burgess, I. J., Step-Scan IR Spectroelectrochemistry with Ultramicroelectrodes: Nonsurface Enhanced Detection of Near Femtomole Quantities Using Synchrotron Radiation. *Analytical Chemistry* **2013,** *85* (18), 8722-8727.
15. Webb, J. A.; Bardhan, R., Emerging advances in nanomedicine with engineered gold nanostructures. *Nanoscale* **2014,** *6* (5), 2502-2530.
16. Bratlie, K. M.; Kliewer, C. J.; Somorjai, G. A., Structure Effects of Benzene Hydrogenation Studied with Sum Frequency Generation Vibrational Spectroscopy and Kinetics on Pt(111) and Pt(100) Single-Crystal Surfaces. *The Journal of Physical Chemistry B* **2006,** *110* (36), 17925-17930.
17. Shao, M.; Yu, T.; Odell, J. H.; Jin, M.; Xia, Y., Structural dependence of oxygen reduction reaction on palladium nanocrystals. *Chemical Communications* **2011,** *47* (23), 6566-6568.
18. Tsuji, M.; Hashimoto, M.; Nishizawa, Y.; Kubokawa, M.; Tsuji, T., Microwave-Assisted Synthesis of Metallic Nanostructures in Solution. *Chemistry – A European Journal* **2005,** *11* (2), 440-452.
19. Jana, N. R.; Gearheart, L.; Murphy, C. J., Wet Chemical Synthesis of High Aspect Ratio Cylindrical Gold Nanorods. *The Journal of Physical Chemistry B* **2001,** *105* (19), 4065-4067.
20. (a) El-Sayed, M. A., Some Interesting Properties of Metals Confined in Time and Nanometer Space of Different Shapes. *Accounts of Chemical Research* **2001,** *34* (4), 257-264; (b) Gai, P. L.; Harmer, M. A., Surface Atomic Defect Structures and Growth of Gold Nanorods. *Nano Letters* **2002,** *2* (7), 771-774.
21. Johnson, C. J.; Dujardin, E.; Davis, S. A.; Murphy, C. J.; Mann, S., Growth and form of gold nanorods prepared by seed-mediated, surfactant-directed synthesis. *Journal of Materials Chemistry* **2002,** *12* (6), 1765-1770.

22. Nikoobakht, B.; El-Sayed, M. A., Preparation and Growth Mechanism of Gold Nanorods (NRs) Using Seed-Mediated Growth Method. *Chemistry of Materials* **2003,** *15* (10), 1957-1962.
23. Xia, Y.; Xia, X.; Peng, H.-C., Shape-Controlled Synthesis of Colloidal Metal Nanocrystals: Thermodynamic versus Kinetic Products. *Journal of the American Chemical Society* **2015,** *137* (25), 7947-7966.
24. Shustorovich, E., Metal-surface reaction energetics: Theory and application to heterogeneous catalysis, chemisorption, and surface diffusion. Wiley-VCH Verlag GmbH: 1991; p 114.
25. Fichthorn, K. A., Atomic-Scale Theory and Simulations for Colloidal Metal Nanocrystal Growth. *Journal of Chemical & Engineering Data* **2014,** *59* (10), 3113-3119.
26. Yang, J.; Lee, J. Y.; Ying, J. Y., Phase transfer and its applications in nanotechnology. *Chemical Society Reviews* **2011,** *40* (3), 1672-1696.
27. Brust, M.; Walker, M.; Bethell, D.; Schiffrin, D. J.; Whyman, R., Synthesis of thiol-derivatised gold nanoparticles in a two-phase Liquid-Liquid system. *Journal of the Chemical Society, Chemical Communications* **1994,** (7), 801-802.
28. Hostetler, M. J.; Wingate, J. E.; Zhong, C.-J.; Harris, J. E.; Vachet, R. W.; Clark, M. R.; Londono, J. D.; Green, S. J.; Stokes, J. J.; Wignall, G. D.; Glish, G. L.; Porter, M. D.; Evans, N. D.; Murray, R. W., Alkanethiolate Gold Cluster Molecules with Core Diameters from 1.5 to 5.2 nm: Core and Monolayer Properties as a Function of Core Size. *Langmuir* **1998,** *14* (1), 17-30.
29. Johnson, S. R.; Evans, S. D.; Brydson, R., Influence of a Terminal Functionality on the Physical Properties of Surfactant-Stabilized Gold Nanoparticles. *Langmuir* **1998,** *14* (23), 6639-6647.
30. Whetten, R. L.; Khoury, J. T.; Alvarez, M. M.; Murthy, S.; Vezmar, I.; Wang, Z. L.; Stephens, P. W.; Cleveland, C. L.; Luedtke, W. D.; Landman, U., Nanocrystal gold molecules. *Advanced Materials* **1996,** *8* (5), 428-433.
31. Di Felice, R.; Selloni, A., Adsorption modes of cysteine on Au(111): Thiolate, amino-thiolate, disulfide. *The Journal of Chemical Physics* **2004,** *120* (10), 4906-4914.
32. Xu, C.; Sun, L.; Kepley, L. J.; Crooks, R. M.; Ricco, A. J., Molecular interactions between organized, surface-confined monolayers and vapor-phase probe molecules. 6. In-situ FTIR external reflectance spectroscopy of monolayer adsorption and reaction chemistry. *Analytical Chemistry* **1993,** *65* (15), 2102-2107.
33. Leff, D. V.; Brandt, L.; Heath, J. R., Synthesis and Characterization of Hydrophobic, Organically-Soluble Gold Nanocrystals Functionalized with Primary Amines. *Langmuir* **1996,** *12* (20), 4723-4730.
34. Turkevich, J.; Stevenson, P. C.; Hillier, J., A study of the nucleation and growth processes in the synthesis of colloidal gold. *Discussions of the Faraday Society* **1951,** *11* (0), 55-75.
35. Sun, S.; Murray, C. B.; Weller, D.; Folks, L.; Moser, A., Monodisperse FePt Nanoparticles and Ferromagnetic FePt Nanocrystal Superlattices. *Science* **2000,** *287* (5460), 1989-1992.
36. Park, J.; An, K.; Hwang, Y.; Park, J.-G.; Noh, H.-J.; Kim, J.-Y.; Park, J.-H.; Hwang, N.-M.; Hyeon, T., Ultra-large-scale syntheses of monodisperse nanocrystals. *Nat Mater* **2004,** *3* (12), 891-895.
37. Lu, X.; Tuan, H.-Y.; Korgel, B. A.; Xia, Y., Facile Synthesis of Gold Nanoparticles with Narrow Size Distribution by Using AuCl or AuBr as the Precursor. *Chemistry – A European Journal* **2008,** *14* (5), 1584-1591.
38. Schmid, G.; Klein, N.; Korste, L.; Kreibig, U.; Schönauer, D., Large transition metal clusters—VI. Ligand exchange reactions on Au55(PPh3)12Cl6—the formation of a water soluble Au55 cluster. *Polyhedron* **1988,** *7* (8), 605-608.
39. Simard, J.; Briggs, C.; Boal, A. K.; Rotello, V. M., Formation and pH-controlled assembly of amphiphilic gold nanoparticles. *Chemical Communications* **2000,** (19), 1943-1944.
40. Sastry, M.; Kumar, A.; Mukherjee, P., Phase transfer of aqueous colloidal gold particles into organic solutions containing fatty amine molecules. *Colloids and Surfaces A: Physicochemical and Engineering Aspects* **2001,** *181* (1–3), 255-259.
41. Nirmala Grace, A.; Pandian, K., Organically dispersible gold and platinum nanoparticles using aromatic amines as phase transfer and reducing agent and their applications in electro-oxidation of glucose. *Colloids and Surfaces A: Physicochemical and Engineering Aspects* **2007,** *302* (1–3), 113-120.

42. Gittins, D. I.; Caruso, F., Spontaneous Phase Transfer of Nanoparticulate Metals from Organic to Aqueous Media. *Angewandte Chemie International Edition* **2001,** *40* (16), 3001-3004.
43. Rucareanu, S.; Gandubert, V. J.; Lennox, R. B., 4-(N,N-Dimethylamino)pyridine-Protected Au Nanoparticles: Versatile Precursors for Water- and Organic-Soluble Gold Nanoparticles. *Chemistry of Materials* **2006,** *18* (19), 4674-4680.
44. Gittins, D. I.; Caruso, F., Biological and Physical Applications of Water-Based Metal Nanoparticles Synthesised in Organic Solution. *ChemPhysChem* **2002,** *3* (1), 110-113.
45. Biver, T.; Corti, A.; Eltugral, N.; Lorenzini, E.; Masini, M.; Paolicchi, A.; Pucci, A.; Ruggeri, G.; Secco, F.; Venturini, M., Analysis of 4-dimethylaminopyridine (DMAP)-gold nanoparticles behaviour in solution and of their interaction with calf thymus DNA and living cells. *J Nanopart Res* **2012,** *14* (2), 1-12.
46. Kang, S. W.; Hong, J.; Park, J. H.; Mun, S. H.; Kim, J. H.; Cho, J.; Char, K.; Kang, Y. S., Nanocomposite membranes containing positively polarized gold nanoparticles for facilitated olefin transport. *Journal of Membrane Science* **2008,** *321* (1), 90-93.
47. Dong, W.-F.; Sukhorukov, G. B.; Mohwald, H., Enhanced Raman imaging and optical spectra of gold nanoparticle doped microcapsules. *Physical Chemistry Chemical Physics* **2003,** *5* (14), 3003-3012.
48. Yu, A.; Liang, Z.; Cho, J.; Caruso, F., Nanostructured Electrochemical Sensor Based on Dense Gold Nanoparticle Films. *Nano Letters* **2003,** *3* (9), 1203-1207.
49. Andreasen, G.; Vela, M. E.; Salvarezza, R. C.; Arvia, A. J., Dynamics of Pyridine Adsorption on Gold(111) Terraces in Acid Solution from in-Situ Scanning Tunneling Microscopy under Potentiostatic Control. *Langmuir* **1997,** *13* (25), 6814-6819.
50. Gandubert, V. J.; Lennox, R. B., Assessment of 4-(Dimethylamino)pyridine as a Capping Agent for Gold Nanoparticles. *Langmuir* **2005,** *21* (14), 6532-6539.
51. Barlow, B. C.; Burgess, I. J., Electrochemical Evaluation of 4-(Dimethylamino)pyridine Adsorption on Polycrystalline Gold. *Langmuir* **2007,** *23* (3), 1555-1563.
52. Vivek, J. P.; Burgess, I. J., Crystallographic dependence of 4-dimethylaminopyridine electrosorption on gold. *Electrochimica Acta* **2013,** *88* (0), 688-696.
53. Rosendahl, S. M.; Danger, B. R.; Vivek, J. P.; Burgess, I. J., Surface Enhanced Infrared Absorption Spectroscopy Studies of DMAP Adsorption on Gold Surfaces. *Langmuir* **2009,** *25* (4), 2241-2247.
54. Danger, B. R.; Fan, D.; Vivek, J. P.; Burgess, I. J., Electrochemical Studies of Capping Agent Adsorption Provide Insight into the Formation of Anisotropic Gold Nanocrystals. *ACS Nano* **2012,** *6* (12), 11018-11026.
55. Lange, H.; Maultzsch, J.; Meng, W.; Mollenhauer, D.; Paulus, B.; Peica, N.; Schlecht, S.; Thomsen, C., Adsorption Behavior of 4-Methoxypyridine on Gold Nanoparticles. *Langmuir* **2011,** *27* (11), 7258-7264.
56. Mollenhauer, D.; Gaston, N.; Voloshina, E.; Paulus, B., Interaction of Pyridine Derivatives with a Gold (111) Surface as a Model for Adsorption to Large Nanoparticles. *The Journal of Physical Chemistry C* **2013,** *117* (9), 4470-4479.

Chapter 2

Experimental Methods and Data Analysis

Molecular adsorption in solution phase modifies the electrical double layer at the solid-liquid interface. Classical electrochemical techniques can be employed to study this interfacial phenomenon by measuring the potential and charge on the metal surface, double layer capacitance and surface pressure of the adsorbed molecular film. In-situ vibrational spectroscopic studies of adsorption at solid-liquid interface can support the electrochemical investigations. In addition, it can provide detailed knowledge about the chemical identity of the adsorbing species and their molecular orientation on the surface. This thesis made use of surface-enhanced infrared absorption spectroscopy (SEIRAS) in addition to the classical electrochemical techniques. Thus a complete description of the monolayer adsorption of MOP molecules is achieved from the macroscopic (thermodynamic) and microscopic (spectroscopic) properties of the reoriented electrode-electrolyte interface. A detailed description of the techniques, methods and data analysis strategies are provided below.

2.1 Electrochemical Set-up

A potentiostat (HEKA PG590) with in-house developed LabView based software was used to perform the electrochemical experiments including cyclic voltametry, differential capacity measurements and chronocoulometry (detailed descriptions of these techniques are provided in the following sections). The data was collected using a multifunction DAQ card (PCI 6251 M Series, National Instuments Corporation, Austin, TX, USA).

2.1.1 Electrochemical Cell

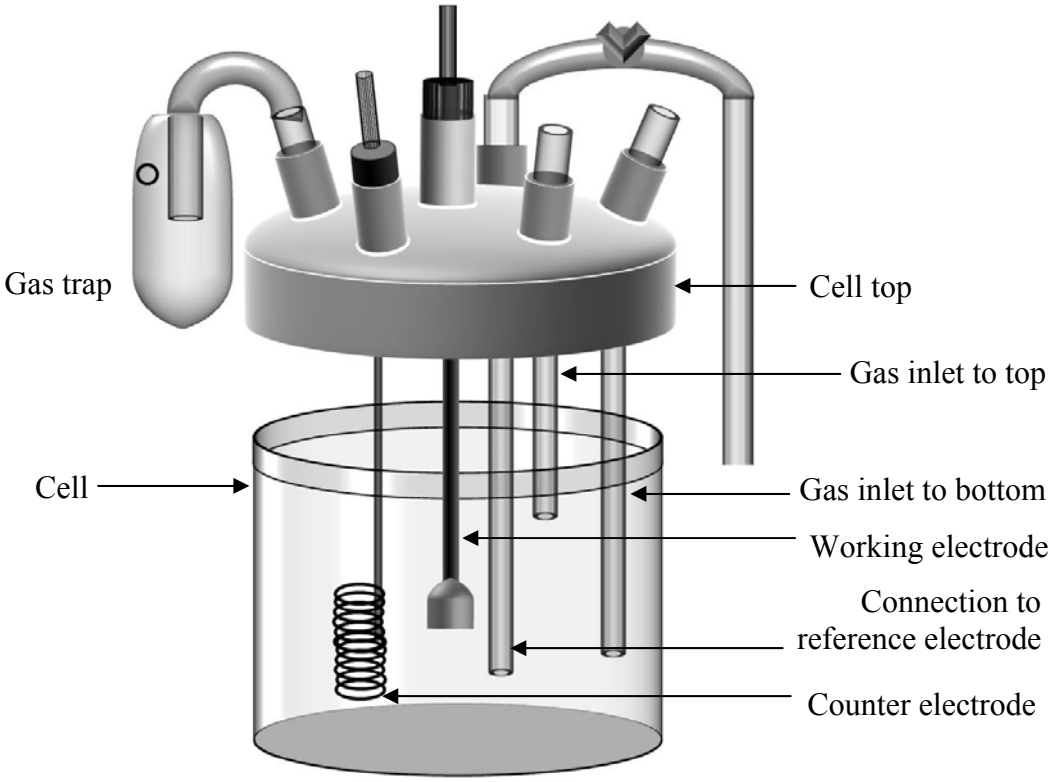

Figure 2.1. Custom made glass cell for electrochemical measurements.

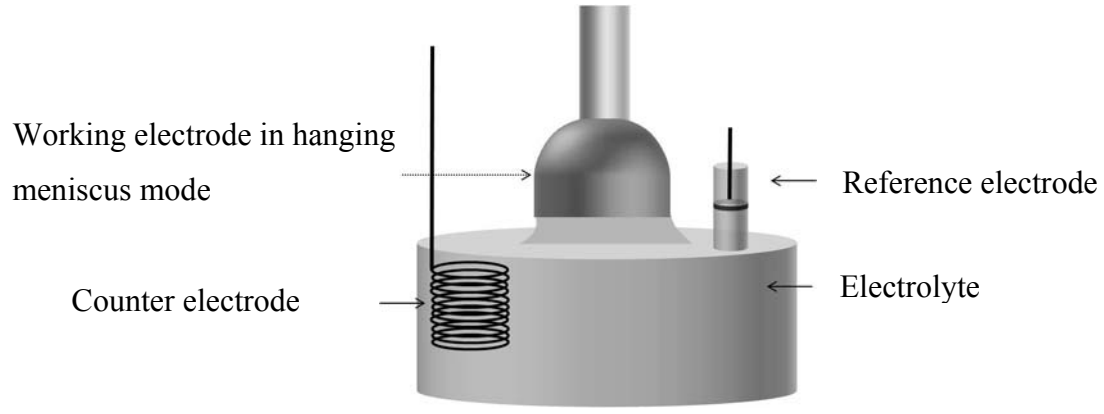

Figure 2.2. Working electrode in hanging meniscus mode.

All the electrochemical measurements were performed using a custom made glass cell (Figure 2.1). The cell set-up consists of a 100 ml glass bottom, a glass top with provisions for the inserting a working electrode, a counter electrode, gas inlets for Ar purging and an exhaust bubbler to minimize the back flow of air into the cell. Before every measurement, the electrochemical glass cell was soaked in a hot acid bath and rinsed with copious amounts of

Milli-Q water. An Ag/AgCl wire immersed in saturated KCl was used as reference electrode and connected to the main cell via a salt bridge to remove the possibility of chloride ion contamination. The electrochemical cell was arranged inside a Faraday cage to avoid any electromagnetic interference from external sources. A coiled gold wire was used as the counter electrode, and the working electrode was connected to the cell in hanging meniscus mode as shown in Figure 2.2.

2.1.2 Single Crystal Au Electrode Preparation

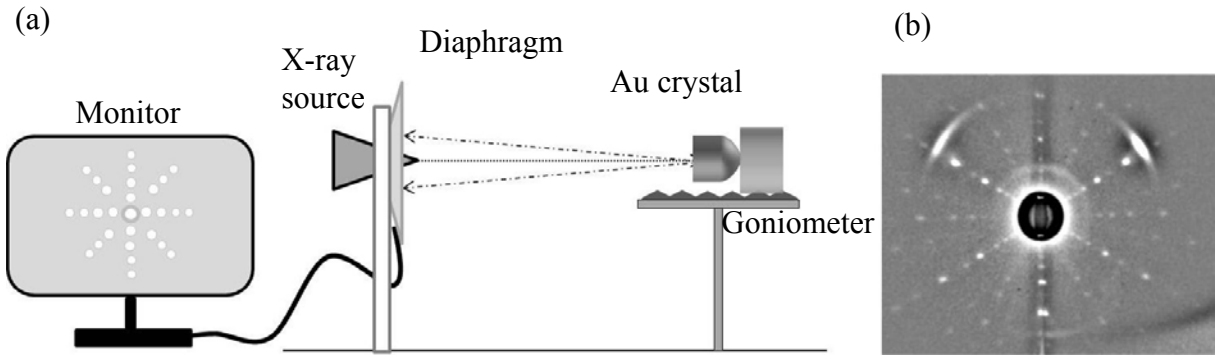

Figure 2.3. (a) Back Laue diffraction set up, (b) X-ray pattern of Au(111).

Metallic gold was melted inside a graphite mould using a programmable induction furnace and cooled in a controlled manner to fabricate the working electrodes with desired shape and crystallinity. The crystalline phase of the electrode was oriented in line with the electrode stem using back Laue X-ray diffraction technique (Figure 2.3. (a)) that provides a stereographic projection of crystal planes. Figure 2.3. (b) shows the characteristic Au(111) X-ray diffraction pattern. Then the electrode was cut along the (111) crystalline plane using successive grades of sandpaper (120, 320, 600 grit) followed by polishing with diamond paste until a mirror finish surface was obtained. The side edge of the Au crystal was also smoothened using diamond paste to avoid electrolyte creeping. The polished Au crystal was treated with piranha solution (1:3 H_2O_2 and H_2SO_4) for 8 hours to remove organic debris

from the metal. Finally, the Au crystal was repeatedly electropolished for five times by anodizing the Au crystal surface by applying required potential potential to obtain 10 mA current, in 5 x 10^{-2} M $HClO_4$ for 30 minutes followed by dissolving the oxide layer in diluted HCl.

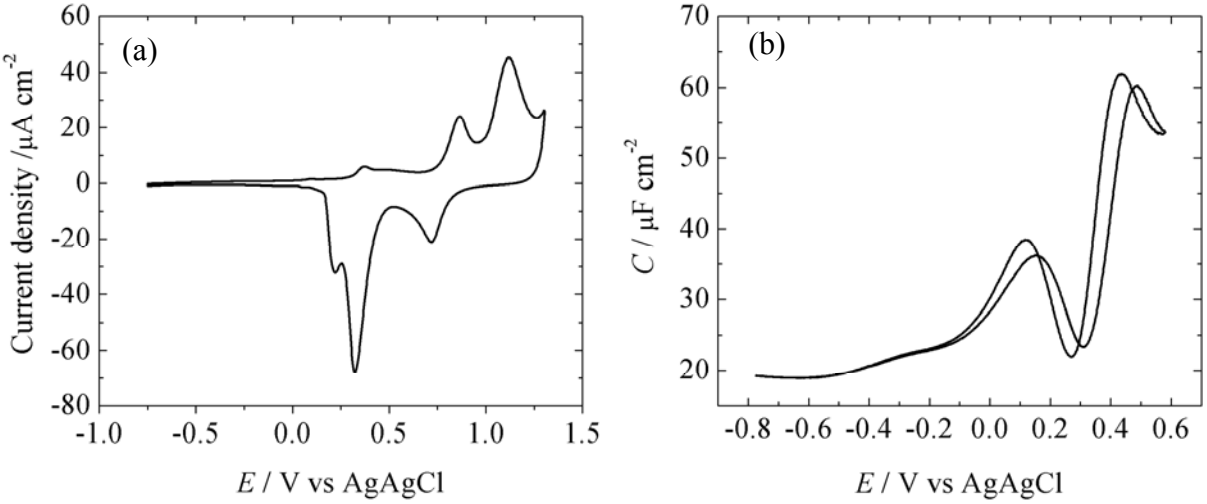

Figure 2.4. (a). Cyclic voltammetry and (b) Differential capacitance of Au (111).

The crystalline character of the electrode was further evaluated by measuring the cyclic voltammetry of the electrode in 5 x 10^{-2} M recrystallized $KClO_4$ and the differential capacity measurement in 5 x 10^{-3} M $KClO_4$. Before the measurements, the electrode was flame annealed to clean and anneal the low index crystal surface. The cyclic voltammetry in Figure 2.4. (a) showed characteristic peaks for the Au (111) and the potential of zero charge (*pzc*) minimum measured using differential capacity was at 0.28 V which was in agreement with literature reports for Au (111) single crystal electrodes as shown in Figure 2.4. (b).[1]

2.2 Cyclic Voltammetry

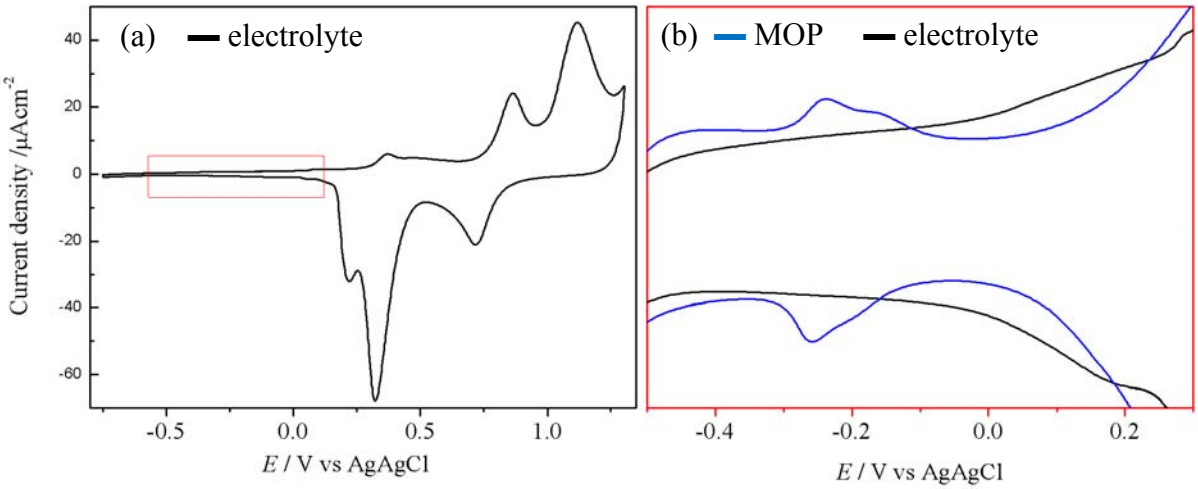

Figure 2.5. (a) The double layer region in the cyclic voltammetry of Au(111) is highlighted in red box, (b) black line represents pure electrolyte and blue line showing adsorption/desorption peaks of surfactant (MOP).

A linear potential sweep (0.02 $V.s^{-1}$) was applied to the working electrode and the charging current at the electrode-electrolyte interface as a function of electrode potential was recorded (Figure 2.5. (a)). The double layer region of the cyclic voltammogram was the region of interest at which no charge transfer occurs during the potential sweep in the pure electrolyte (Figure 2.5. (b)). The potential window of double layer region depends on the electrolyte pH. In 5 x 10^{-2} M $KClO_4$, where the pH is neutral, the double layer region appears between approximately -0.60 V and 0.50 V. The surfactant in the electrolyte showed characteristic adsorption/desorption peaks in the double layer region. Thus, the cyclic voltammetry provided information regarding the potential window at which the molecule of interest (MOP in this work) adsorbs on the electrode surface.

2.3 Differential Capacitance Measurement

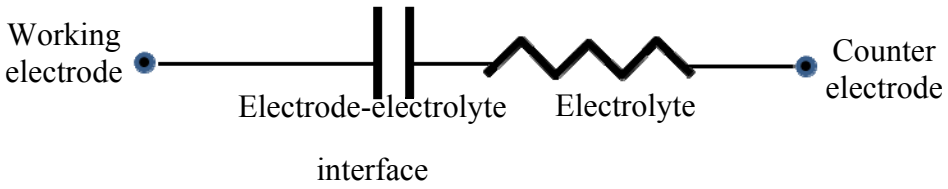

Figure 2.6. Diagram showing an equivalent electrical circuit for electrochemical cell.

The differential capacity (DC) measurement was used to probe the processes occurring at the electrode-electrolyte interface which can modelled as an equivalent circuit consisting of a resistor and a capacitor in series (Figure 2.6.). The resistive element represents the ionic conduction of electrolyte species and the capacitor represents the ideally polarized electrode's ability to store charge. By considering the compact electrical double layer as a parallel plate capacitor, the capacitance (C) can be equated as

$$C = \frac{A\,\varepsilon_0\varepsilon_r}{d} \qquad \textbf{Eq 2.1}$$

where A is the plate area, $\mathcal{E}_0$ is the permittivity of free space, $\mathcal{E}_r$ is the relative permittivity, and d is the thickness of the inner part of the electrical double layer which equates roughly to the size of the molecules adsorbed on the electrode surface. Upon adsorption of organic molecules by replacing the water molecules at the metal-solution interface, the capacitance value lowers due to the decrease in the refractive index of adsorbed molecules. In addition to that, the increase in the thickness of inner Helmholtz plane due to the fact that organic molecules tend to be larger than water molecules will also decrease the capacitance. The differential capacity of the double layer is defined as

$$C = \left(\frac{\partial\sigma_m}{\partial\Gamma}\right)_E \frac{\partial\Gamma}{\partial E} + \left(\frac{\partial\sigma_m}{\partial E}\right)_\Gamma \qquad \textbf{Eq 2.1}$$

where σ_m is the metal charge density at the electrode surface which is a function of electrode potential (E) and the Gibbs surface excess (Γ). In the DC measurement (alternating current

(*ac*)-voltammetry) technique, a sinusoidal perturbation (5.0 x 10^{-3} V, 25 Hz) was superimposed on the direct current (*dc*) voltage during the potential sweep. The resulting current with real (Re) and imaginary (Q) components was acquired using a lock-in-amplifier and converted into *dc* potential dependent capacitance values assuming a series equivalent circuit of a resistor and a capacitor. The former models the electrolyte's resistance and the latter the double layer of the electrode-solution interface. Hence the differential capacity (C) can be determined from the following equation without an independent determination of the solution resistance

$$C = \frac{Q}{E_{ac}} \times \frac{1}{\omega} \times \left[1 + \left(\frac{Re}{Q}\right)^2\right] \qquad \textbf{Eq 2.2}$$

where E_{ac} is the root mean square voltage and ω is the angular frequency of the ac perturbation.

2.4 Chronocoulometry

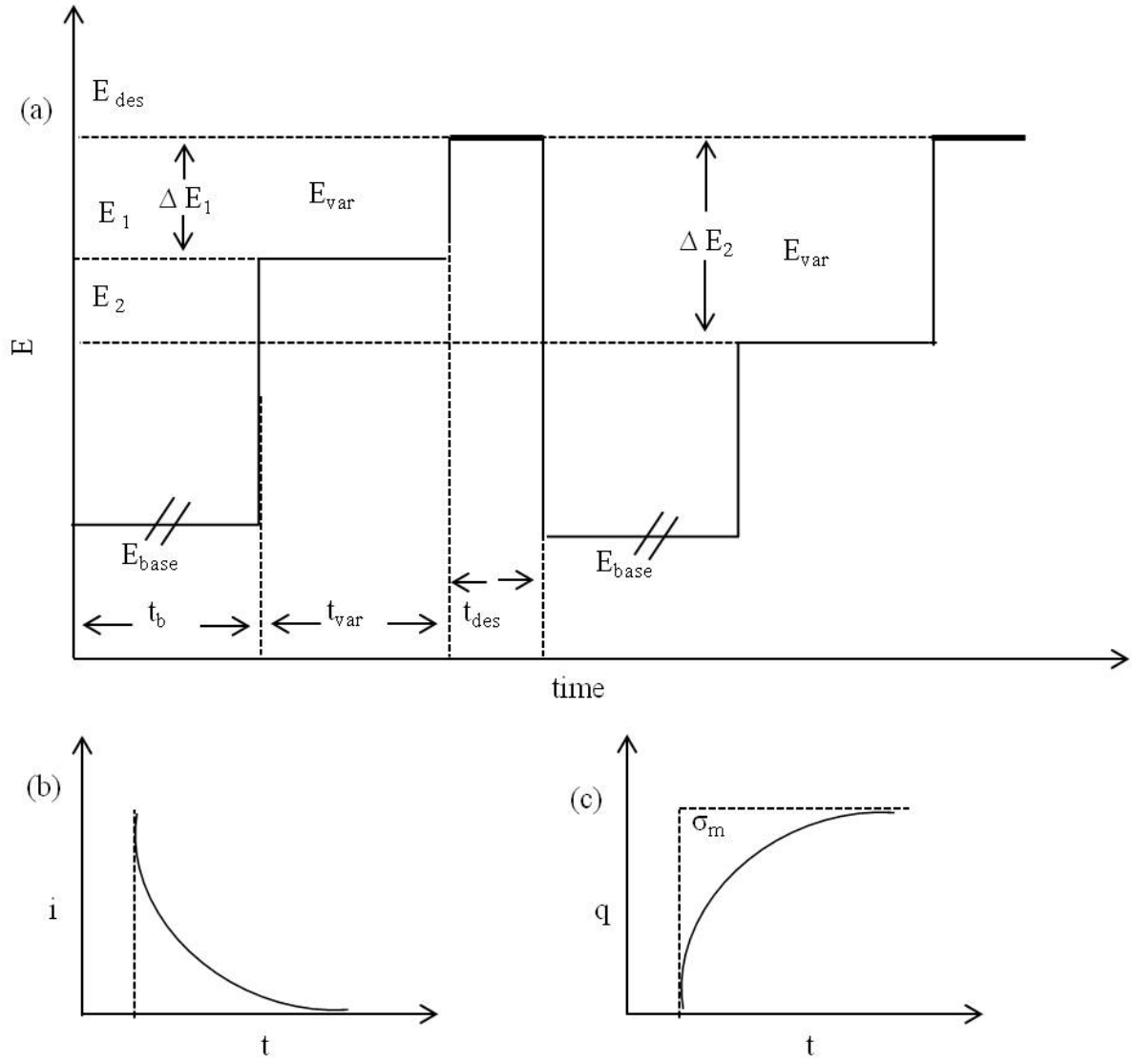

Figure 2.7. (a) Schematic representation of chronocoulometry steps , (b) current transient, (c) charge transient.

In chronocoulometry (CC), the charge at the electrode surface is measured as a function of time. Figure 2.7. (a) shows the schematic representation of CC experiment with the following steps: an initial base potential (E_{base}), where the film of adsorbed molecules remains stable, was applied to the working electrode. Then the electrode potential was stepped to a variable potential (E_{var}) for a specific amount of time (t_{var}) sufficient to achieve an adsorption equilibrium at the electrode-electrolyte interface. Then the electrode potential was once again

shifted to the desorption potential (E_{des}), previously determined from the DC curves. The current flowing to the interface during this step was acquired as a function of time, and then the electrode potential was stepped back to E_{base}. The measurement was repeated for different values of E_{var}. Figure 2.7. (b) represents a typical current transient where the current decays exponentially with time. The current transient can be integrated to obtain the charge transients as shown in Figure 2.7. (c). Extrapolation of the long time charge transients back to zero time provides the total surface charge density, σ_m for a given *dc* potential, E_{var}. Current transients were collected for different E_{var} to obtain the total surface charge density (σ_m) as a function of potential.

2.5 Derivation of the Equation for Surface Pressure (Π) from General Electrocapillary Equation

Surface tension is the phenomenon that results from the asymmetric cohesive forces experienced by the liquid molecules at the interface. Molecular adsorption on the surface can alter the surface tension; hence measurement of surface tension can provide useful information about the extent of molecular adsorption at the interface (or the Gibbs surface excess). But there is no direct method to measure surface tension at the solid-liquid interface. However the surface pressure of the adsorbed film (Π), which is the difference in surface tension with and without molecular adsorption, can be measured from the charge density data (equation 2.15) obtained through chronocoulometry. It is possible to extract the Gibbs surface excess from surface pressure values as described in the following thermodynamic treatments.[2]

The acid dissociation equilibrium for the model molecule, Py, can be expressed as

$$PyH^+ \rightleftharpoons Py(aq) + H^+(aq) \qquad K_a^* \qquad \textbf{Eq 2.4}$$

where K_a^* is the acid equilibrium constant that differs numerically from the acid equilibrium concentration ratio, K_a , typically reported for organic acids, i.e. $K_a^* = \frac{K_a}{55.5M}$ (where 55.5 M is the molarity of water).

The acid equilibrium expression can be written in terms of mole fractions (χ) of the base (Py) and conjugate acid (PyH^+) forms of the model molecule and χ^o is the standard state mole fractions of corresponding species.

$$K_a^* = \frac{\left(\chi_{Py} / \chi_{Py}^o\right)\left(\chi_{H^+} / \chi_{H^+}^o\right)}{\left(\chi_{PyH^+} / \chi_{PyH^+}^o\right)} \qquad \textbf{Eq 2.5}$$

in which,

$$\chi_{Py} = \frac{\chi_F}{1+\beta\chi_H} \qquad \textbf{Eq 2.6}$$

where $\beta = \frac{\chi_{PyH^+}^o}{\chi_{Py}^o \chi_{H^+}^o K_a^*}$ and the formal mole fraction, χ_F is $\chi_F = \chi_{Py} + \chi_{PyH^+}$

A general electrocapillary equation can be written for a non-adsorbing electrolyte containing both forms of the molecule

$$-d\gamma = \sigma_m dE + \boldsymbol{\Gamma}_{Py} d\mu_{Py} + \boldsymbol{\Gamma}_{PyH^+} d\mu_{PyH^+} + \boldsymbol{\Gamma}_{H^+} d\mu_{H^+} \qquad \textbf{Eq 2.7}$$

where γ is the interfacial surface tension, σ_m is the electronic charge density of the metal, E is the electrode potential and Γ represents the Gibbs surface excess of a given species. The chemical potential, μ, of Py is written in terms of its mole fraction and its activity coefficient g as

$$\mu_{Py} = RT \ln\left[g_{Py} \frac{\chi_{Py}}{\chi^0_{Py}} \right] \qquad \textbf{Eq 2.8}$$

After substituting the expression for χ_{Py} in equation 2.6 in equation 2.8, the incremental change in the chemical potential of Py can be expressed as

$$d\mu_{Py} = RTd\chi_F + RTd \ln\left[\frac{g_{Py}}{\chi^0_{Py}} \frac{1}{1+\beta\chi_H} \right] \qquad \textbf{Eq 2.9}$$

Under conditions of constant pH and constant ionic strength, the last term contains only constants and will have no differential change as a function of χ_F

$$d\mu_{Py} = RTd\chi_F \qquad \textbf{Eq 2.10}$$

Similarly, the chemical potential of PyH^+ can be expressed in terms of χ_F

$$\mu_{PyH^+} = RT \ln\left[g_{PyH^+} \frac{\chi_{PyH^+}}{\chi^0_{PyH^+}} \right] = RT \ln\left[g_{PyH^+} \frac{\chi_F - \chi_{Py}}{\chi^0_{PyH^+}} \right] \qquad \textbf{Eq 2.11}$$

Substituting equation 2.6 in 2.11 leads to

$$d\mu_{PyH^+} = RTd \ln \chi_F + RTd \ln\left[\frac{g_{PyH^+}}{\chi^0_{PyH^+}} \left(1 - \frac{1}{1+\beta\chi_H} \right) \right] \qquad \textbf{Eq 2.12}$$

As before the last term reduces to zero for conditions of constant pH and constant ionic strength and the expression obtained simplifies to

$$d\mu_{PyH^+} = RTd\ln\chi_F \qquad \textbf{Eq 2.13}$$

Equations 2.10 and 2.13 can be used to re-write 2.5.4 under conditions of constant pH and constant ionic strength

$$-d\gamma = \sigma_m dE + \left(\Gamma_{Py} + \Gamma_{PyH^+}\right) d\ln\chi_F \qquad \textbf{Eq 2.14}$$

The difference in interfacial tension for the interface in the absence and presence of Py-derivative can be defined as $\Pi = \gamma_{\chi_F=0} - \gamma_{\chi_F}$ and can be calculated by integrating charge-density versus potential plots under conditions of constant electrolyte composition

$$\Pi = \left[\int_{E_{des}}^{E} \sigma_M dE\right]_{\chi_F} - \left[\int_{E_{des}}^{E} \sigma_M dE\right]_{\chi_{F=0}} \qquad \textbf{Eq 2.15}$$

In the absence of specifically adsorbed species, the interfacial tension in the electrolyte is a constant $d\Pi = -d\gamma_{\chi_F}$ and under conditions of constant potential, equation 2.14 can be re-written to form an expression for the total surface excess of the adsorbed species in terms of the surface pressure and the formal concentration of the model molecule in the electrolyte

$$\left(\Gamma_{Py} + \Gamma_{PyH^+}\right) = \frac{1}{RT}\left[\frac{\partial\Pi}{\partial\ln\chi_F}\right]_E \qquad \textbf{Eq 2.16}$$

By analogy with the thermodynamic information available for DMAP adsorption it is known that the surface excess of the conjugate acid is zero.[3] Thus, equation 2.16 can be rewritten as

$$\Gamma_{Py} = \frac{1}{RT}\left[\frac{\partial \Pi}{\partial \ln \chi_F}\right]_E \qquad \textbf{Eq 2.17}$$

2.6 Methodology for the Determination of Thermodynamic Parameters

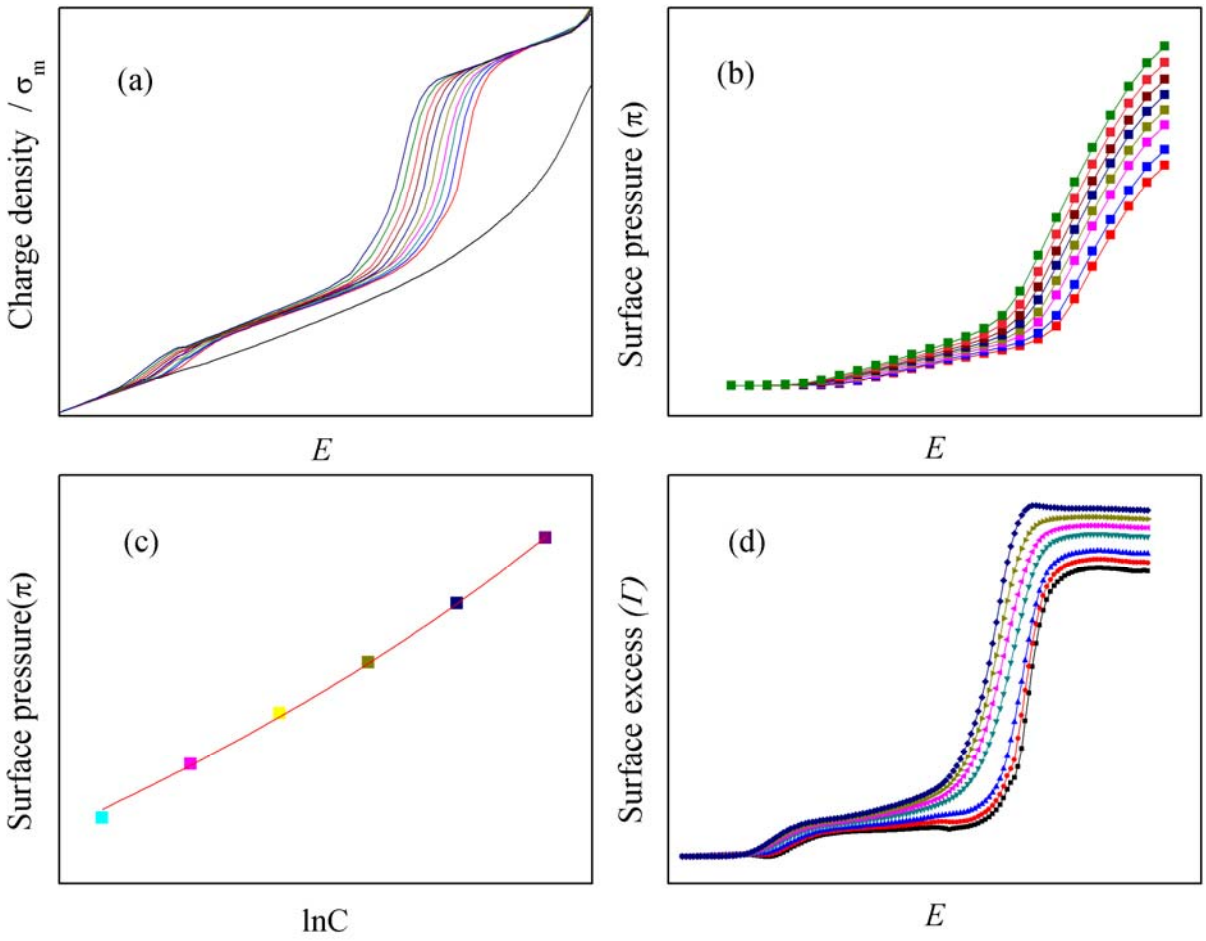

Figure 2.8. (a) Charge density data obtained from current transients for a variety of adsorbant concentrations, (b) Surface pressure plot obtained from charge density, (c) Surface pressure as function of adsorbant concentration and (d) surface excess as a function of electrode potential.

Figure 2.8. outlines the representative steps involved in the determination of the Gibbs surface excess. Figure 2.8. (a) shows the charge density data as a function of electrode potential obtained for the increasing concentration of adsorbates (e.g. MOP) in the electrolyte solution. The area between the charge density curve for each concentration and the pure electrolyte equals the surface pressure (Π) of the electrode surface at that concentration. Figure 2.8. (b) represents the Π values at corresponding electrode potentials for an increasing

concentration of adsorbing molecules in the electrolyte. As decribed above, the surface pressure is determined by numerical integration of the charge density versus potential plots

$$\Pi(E) = \left[\int_{E_0}^{E} \sigma_m dE\right]_c - \left[\int_{E_0}^{E} \sigma_m dE\right]_{c=0} \qquad \textbf{Eq 2.18}$$

Next, the Π values at constant electrode potentials can be plotted against logarithmic values of adsorbate concentration in the electrolyte (Figure 2.8. (c)). These curves were differentiated and divided by RT to get the Gibbs excess (Γ) and expressed as a function of potential (equation 2.17).

2.7 Infrared Spectroelectrochemical Set-up

The SEIRAS spectra were collected using a Bruker VERTEX 70 FT-IR spectrometer equipped with liquid nitrogen cooled mercury cadmium telluride (LN-MCT) Photovoltaic AC detector. The spectra were stored from 4000 cm^{-1} to 1000 cm^{-1}, with a resolution of 4 cm^{-1} and each spectrum was calculated from 128 interferometric scans. The optic box inside the spectrometer was constantly purged with CO_2-free dry air from a Parker Balston FT-IR purge gas generator 75-62 (Parker Hannifin Corporation, Haverhill, MA). The electrode potential in the spectroelectrochemical cell was controlled using a HEKA potentiostat (HEKA PG590).

2.7.1 Spectroelectrochemical Cell Assembly

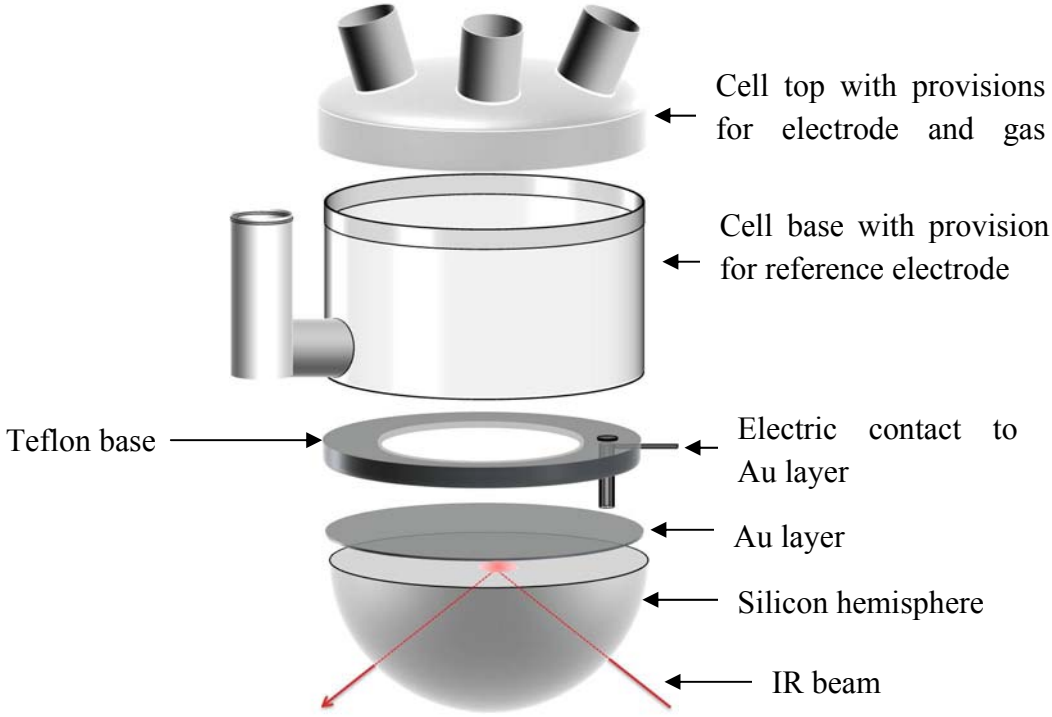

Figure 2.9. The spectroelectrochemical cell in Kretschmann configuration.

All the SEIRAS measurements were performed in attenuated total reflectance mode using a spectroelectrochemical cell in the Kretschmann configuration (Figure 2.9.).[4] A 25 mm diameter silicon hemisphere coated with gold (see below) was used as the working electrode. Before the gold deposition, the silicon hemisphere was polished with diamond polishing suspensions (initially with 3 μm and then with 0.5 μm) and then cleaned ultrasonically with ethanol (95%) and Milli-Q water. An Ag/AgCl in saturated KCl was used as the reference electrode and connected to the spectroelectrochemical cell via a salt bridge. A flame annealed gold coil was used as the counter electrode. Before the measurements, the electrolyte solution was degassed for 30 minutes and an argon blanket was maintained inside the cell throughout the experiment.

2.7.2 Fabrication of Thin Film Au Electrode

The Au layer on the silicon hemisphere was made through the thermal deposition technique. Prior to the Au deposition, the polished Si hemisphere surface was treated with NH_4F buffer solution for 60 seconds to remove the surface oxide layer on the Si.[5] Then the Si hemisphere was transferred into a vacuum chamber. The Au was deposited onto the Si hemisphere at a rate of 0.01 Å/sec while the chamber pressure was maintained at 10^{-6} mTorr. The deposition was continued until the Au film thickness reached ~30 nm. The Au layer on the silicon hemisphere was electrochemically polished by cycling the potential between the 0.10 V to 1.20 V in 50 mM NaF at a sweep rate of 0.02 $V.sec^{-1}$ for 30 minutes.

2.7.3 Potential Dependent IR Data Acquisition Protocol

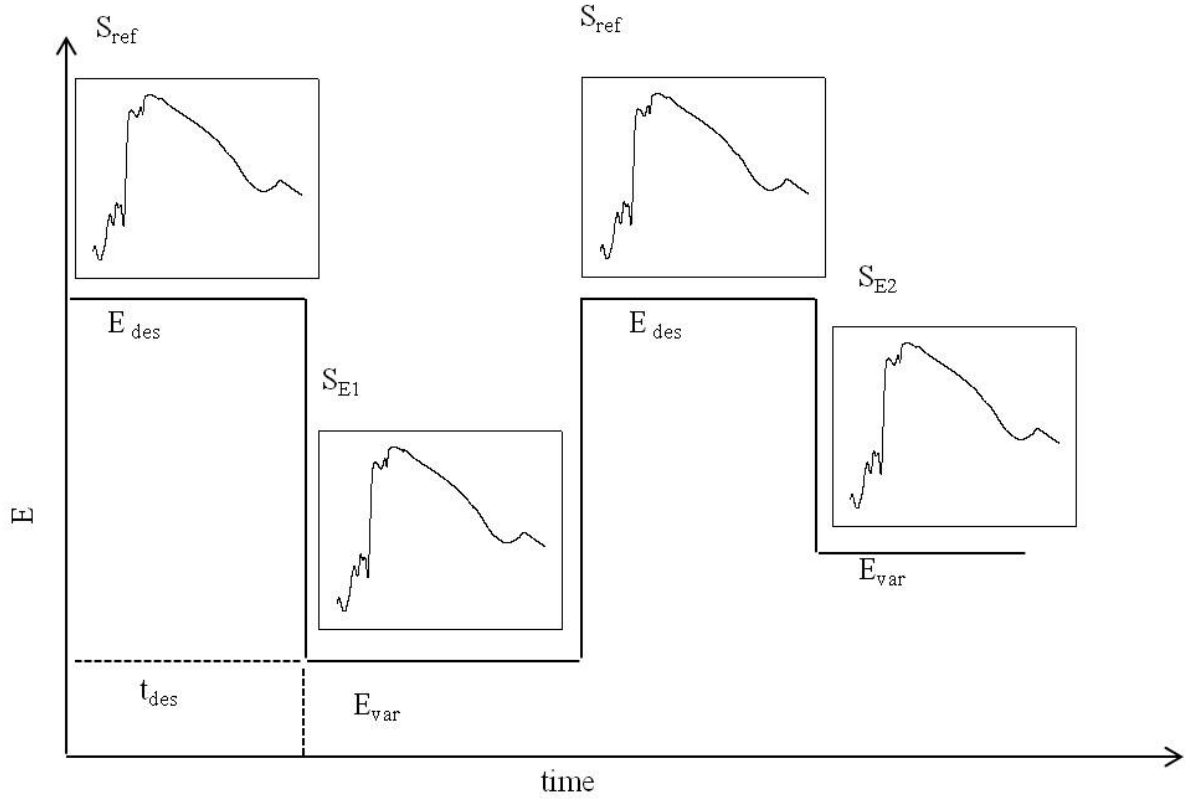

Figure 2.10. Schematic representation of potential dependent IR data acquisition protocol.

An in-house developed LabVIEW (National Instruments) program was used to control the FT-IR spectrometer and the potentiostat while performing the potential-dependent SEIRAS experiments. The initial applied potential was adjusted to the open circuit potential (ocp) of the Au film in the SEIRAS cell. Then the applied potential was switched to -0.70 V and maintained for 10 seconds to desorb the molecules from Au surface. An IR spectrum was collected at the desorption potential which serves as the reference spectrum (S_{ref}). The electrode potential was stepped to 0.50 V (first variable step potential) and the potential was maintained for 45 seconds to reach adsorption equilibrium before collecting the next IR spectrum (S_{var}). S_{var} was collected for every variable potentials ranging from 0.50 V to -0.60 V and a corresponding S_{ref} was also collected for every S_{var} .

The resultant spectrum were initially calculated as the ratio of the difference between the IR spectrum at variable potential and reference spectrum to the reference spectrum.

$$\text{Resultant spectra} = \frac{S_{var} - S_{ref}}{S_{ref}} \qquad \textbf{Eq 2.19}$$

The final spectra are expressed in terms of absorbance (Abs), where

$$Abs = -log_{10}\left[\frac{S_{var} - S_{ref}}{S_{ref}}\right]^{-1} \qquad \textbf{Eq 2.20}$$

The upward peaks in the IR absorbance spectra represent the energy absorption due to the molecular vibration of MOP functional moieties at corresponding IR frequencies.

References

1. Stolberg, L.; Morin, S.; Lipkowski, J.; Irish, D. E., Adsorption of pyridine at the Au(111)-solution interface. *Journal of Electroanalytical Chemistry and Interfacial Electrochemistry* **1991,** *307* (1–2), 241-262.
2. Lipkowski, J.; Stolberg, L., Adsorption of molecules at metal electrodes. Lipkowski, J.; Ross, P. N., Eds. VCH: 1992; pp 171-238.
3. Rosendahl, S. M.; Danger, B. R.; Vivek, J. P.; Burgess, I. J., Surface Enhanced Infrared Absorption Spectroscopy Studies of DMAP Adsorption on Gold Surfaces. *Langmuir* **2009,** *25* (4), 2241-2247.
4. Hatta, A.; Chiba, Y.; Suëtaka, W., Infrared absorption study of adsorbed species at metal/water interface by use of the Kretschmann configuration. *Surface Science* **1985,** *158* (1–3), 616-623.
5. Delgado, J. M.; Orts, J. M.; Pérez, J. M.; Rodes, A., Sputtered thin-film gold electrodes for in situ ATR-SEIRAS and SERS studies. *Journal of Electroanalytical Chemistry* **2008,** *617* (2), 130-140.

Chapter 3

Electrochemical Investigation of 4-Methoxypyridine Adsorption on Au(111)

3.1 Introduction

A thorough understanding of the interaction of between the metal surface and molecular stabilizers is imperative for formulating procedures to synthesize nanoparticles (NPs) with predetermined shape and size. The ligand-metal interaction during the NP formation can be mimicked on an electrode surface by electrosorbing ligand molecules on a charged metal surface. Therefore, electrochemical methods can provide an ideal platform to study the adsorption behaviour of molecules at the solid-liquid interface.

Studies on reversible adsorption of molecules at surfaces of metals like gold and silver display a broad range of potentials at which the metal-liquid interface is nearly ideally polarizable (double layer region).[1] The surface crystallography of the metal strongly influences the double layer properties. The molecular adsorption studies of organic molecules on Group 1B metals in the gas phase implies that the metal-adsorbate interaction can be classified as weak chemisorption involving the adsorbates molecular orbitals and the metal's electronic states. Molecular adsorption on Group 1B metals can be studied using electrochemical techniques and fundamentally significant thermodynamic information related to adsorption at the solid-liquid interface can be extracted. Lipkowski *et al*. developed a chronocoulometric technique for determining charge density at solid electrodes.[2] They provided thermodynamic treatments to acquire quantitative information regarding the molecular adsorption on Au and Ag electrodes (See Chapter 2 Section 2.4 and 2.5 for details).

The Burgess group has utilized the chronocoulometry technique to study the adsorption properties of 4-dimethylaminopyridine (DMAP) on different Au crystal planes.[3,4] The same

strategy is adopted in the current chapter to learn about the adsorption behaviour of 4-methoxypyridine on Au surface. This study is an important step towards the screening process of ligands suitable for anisotropic nanoparticle synthesis.

3.2 Experimental

3.2.1 Reagents, Solutions and Electrode Materials

All the chemicals including 4-methoxypyridine (MOP) (97%), potassium perchlorate ($KClO_4$) (+99%) and perchloric acid ($HClO_4$) (70%) were purchased from Sigma-Aldrich. Diethyl ether anhydrous (≥ 99%, BHT stabilised) was purchased from Fisher Scientific. Potassium perchlorate was used after double recrystallization from Milli-Q (≥18.2 MΩ.cm) water and all the other chemicals were used as received. 4-Methoxypyridinium perchlorate ($MOP.HClO_4$) was obtained by the dropwise addition of neat MOP into the concentrated $HClO_4$. The white-coloured, spike-like $MOP.HClO_4$ crystals were dissolved in Milli-Q water and precipitated with diethyl ether. The $MOP.HClO_4$ crystals were collected on a fine frit, vacuum dried and stored in a vacuum sealed desiccator. All aqueous solutions were made using Milli-Q water. A detailed description of the fabrication of single crystal gold electrodes including methods used to grow, orient, cutting and polishing the crystals is provided in Chapter 2.

3.2.2 Electrochemical Measurements and Instrumentation

All the electrochemical measurements were carried out in an in-house designed glass cell set-up, and working electrode was connected to the electrochemical cell in hanging meniscus configuration. Before each electrochemical measurement, all the glassware was cleaned through the following optimized process. Glassware was immersed in a hot acid bath (3:1 mixture of H_2SO_4 and HNO_3) for 30 minutes. After cooling down, the acid was rinsed off with a copious amount of Milli-Q water and the whole electrochemical cell was soaked in Milli-Q water overnight. The glass cell was thoroughly rinsed again before use. A flame

annealed gold coil was used as the counter electrode and Ag/AgCl in saturated KCl as the reference electrode, which was connected to the cell via a salt bridge. The crystalline gold working electrode was also flame annealed, cooled in air and by Milli-Q water before each electrochemical measurements. The electrolyte solution (5 x 10^{-2} M $KClO_4$) was degassed for at least 30 minutes with argon before the experiments. An argon gas blanket was maintained inside the cell during the experiments, and the cell temperature was 20±2 ^{o}C. The pH of the electrolyte solution was adjusted to the desired values using dilute $HClO_4$ solution prior to the experiments. A spiking solution of MOP/H^+ was made with MOP and MOP.$HClO_4$ at required ratio to maintain a constant pH of the electrolyte while performing the pH dependent electrochemical measurements. For experiments performed at pH 4, the MOP solution was made with only MOP.$HClO_4$. The electrochemical measurements were carried out using a HEKA PG590 potentiostat (HEKA, Mahone Bay, NS, CA) and an SR830 DSP lock-in amplifier (Stanford Research Systems, Sunnyvale, CA). For differential capacitance experiments, an *ac* perturbation of 5 x 10^{-3} V, 25 Hz was superposed to the 5 x 10^{-3} V.s^{-1} *dc* sweep.

3.3 Results and Discussion

Detailed differential capacitance studies of MOP adsorption at pH = $pK_{a,\ MOPH+}$ = 6.5 [5] and pH = 4 were conducted on Au(111) and Au(polycrystalline) electrodes to learn the crystallographic dependence of MOP adsorption. The thermodynamic information about the adsorption behaviour of DMAP on Au(111) electrodes at pH = $pK_{a,\ DMAPH}^{+}$ = 9.7 is available from the previous studies done by the Burgess group.[4] An analogous study with MOP at pH = $pK_{a,\ MOPH}^{+}$ = 6.5 is performed here to compare and contrast the adsorption features of these two pyridine derivatives.

3.3.1 Differential capacitance of MOP on Au electrodes

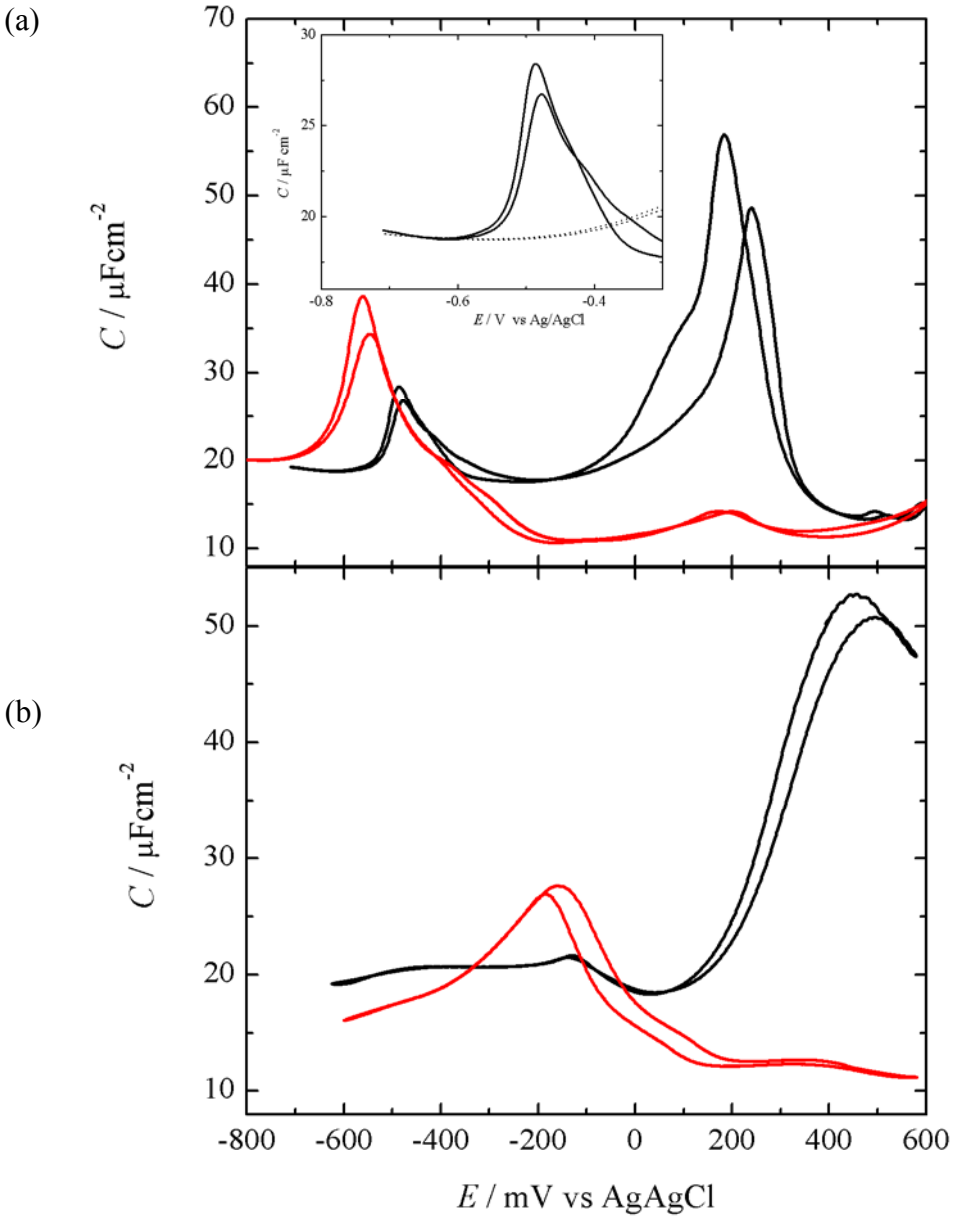

Figure 3.1. Differential capacity curves for MOP adsorption at a) pH 6.5 and b) pH 4 of Au(111) (—), and Au(polycrystalline) (—). Inset figure shows merging of pure electrolyte (····) with MOP on Au(111) at desorption potential.

The differential capacity for both Au crystal electrodes were first measured in pure electrolyte at pH 6.5 and then at MOP/H^+ (5 x 10^{-5} M) as shown in Figure 3.1 (a). At the most negative potentials (between -0.70 V and -0.80 V), the capacitance curve of MOP/H^+ (5 x 10^{-5}

M) merges with the capacitance curve of the pure electrolyte (5 x 10^{-2} M $KClO_4$) which depicts the complete desorption of all MOP species from the electrode surface (inset Figure 3.1 (a)). The capacitance value measured at the desorption potential of MOP/H^+ on Au(111) is 19 $\mu F.cm^{-2}$. The presence of two plateaues seperated by a pesudocapacitive peak is a typical feature of two states of adsorption, which is also reported in the case of pyridine.[4, 6] The capacitance value of the first plateau (-0.50 to -0.10 V) is 18 $\mu F.cm^{-2}$ and that of the second plateau (0.10 and 0.30 V) is 11 $\mu F.cm^{-2}$. The inner Helmholtz layer will be thinner when the molecules adsorb horizontal to the electrode surface and the Helmholtz layer become thicker during vertical orientation of the adsorbates. Since the interfacial capacitance is inversely proportional to the inner Helmholtz layer thickness, it is likely that the former capacitance plateau belongs to π-bonded (horizontal state) adsorption of MOP, and the later one belongs to σ-type orientation (vertical state) of MOP molecules involving the ring nitrogen. The former pseudocapacitive peak in the DC curves represents the onset of MOP adsorption, and the later peak indicates phase transition between the adsorption states I and II.[♣]

There are significant differences in the adsorption features of MOP on single crystalline and poly crystalline surfaces as shown in Figure 3.1 (a) and (b). Therefore, like DMAP, MOP adsorption is also crystallographic dependent. Au(polycrystalline) surfaces (red solid lines) shows only one capacitive minimum (~ 10 to 12 $\mu F.cm^{-2}$) at pH = $pK_{a,\ MOPH+,}$ which is comparable to the capacitive values of state II adsorption. This concludes that MOP favours

---

[♣] π-bonded (horizontal state) orientation will be mentioned as 'state I' and σ-type orientation (vertical state) will be mentioned as 'state II' adsorption.

MOP/H^+ stands for equilibrium mixture of base and protonated form of MOP

state II adsorption on high-index crystal surfaces compared to Au(111) over a large range of electrode potentials at pH = $pK_{a,\ MOPH+}$. The presence of pseudocapacitance peak for polycrystalline Au at positive potentials (~0.20 V) at neutral pH is the result of relatively larger (111) character of polycrstalline electrode.

In addition to surface crystallography, MOP adsorption critically depends upon the solution pH. Figure 3.1 (b) shows at acidic condition (pH = 4) MOP adopts only the horizontal state adsorption and forms a low-capacity film on Au(111) over the entire potential range. Meanwhile, it is evident from DC curves that MOP exhibits two state adsorption on Au(polycrystalline) at the same acidic pH.

3.3.2 Chronocoulometry

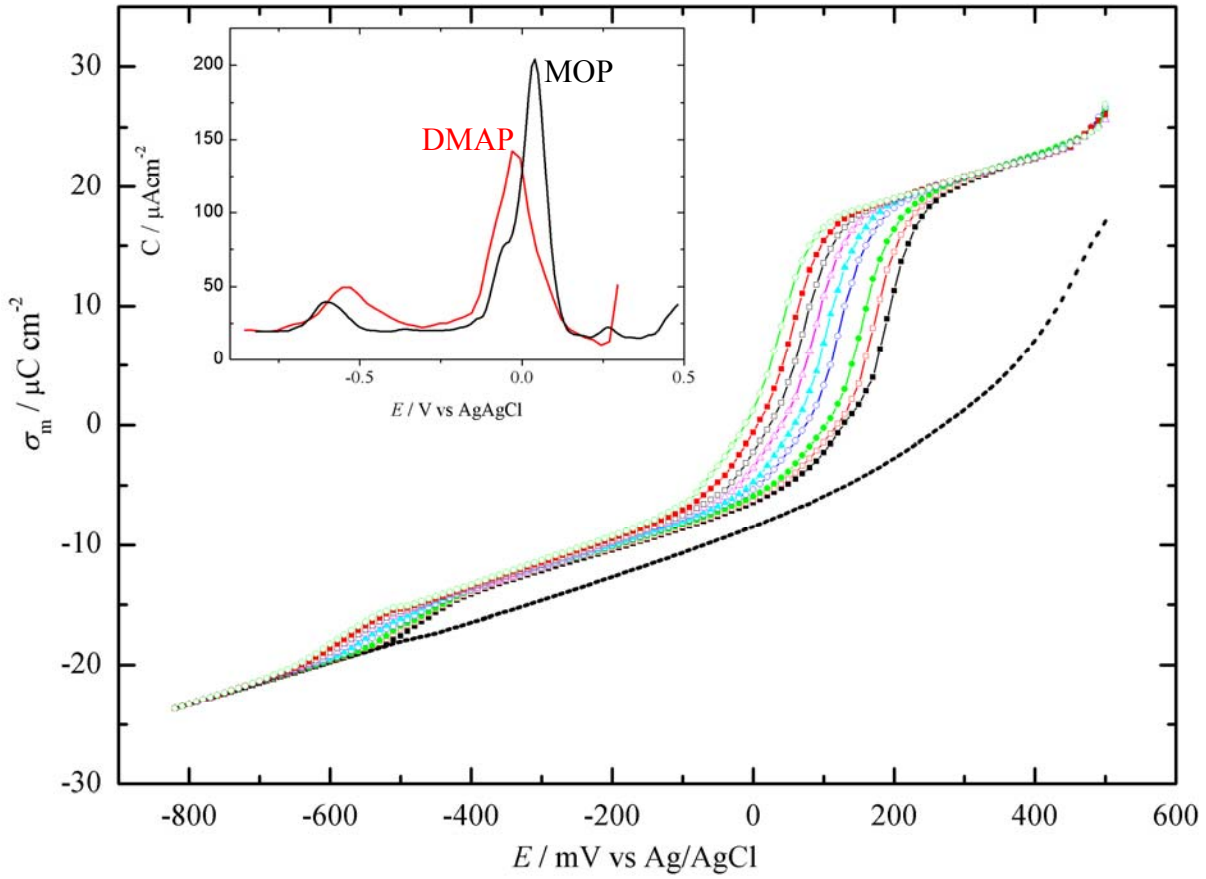

Figure 3.2. Charge density versus electrode potential plots obtained from chronocoulometry experiments on Au(111) in 5 x 10^{-2} M $KClO_4$ ($pH_{electrolyte}$ = $pK_{a,\ MOPH+}$ = 7) and varying formal concentrations of MOP (5.0 x 10^{-5} M (■), 7.0 x 10^{-5} M (□), 1.0 x 10^{-4} M (●), 1.9 x 10^{-4} M (○), 2.6 x 10^{-4} M (▲), 3.7 x 10^{-4} M(Δ), 5.1 x 10^{-4} M(□), 7.2 x 10^{-4} M (■) and 1.0 x 10^{-3} M (○). Dotted line represents the supporting electrolyte. Inset figure shows the differential capacity curves of MOP (—) and DMAP (—) on Au (111) at pH = pK_a of the corresponding protonated organic species.

The details about chronocoulometry measurements and the method to determine absolute charge density (σ_m) are discussed in Chapter 2. Figure 3.2 shows charge density plots for 5 x 10^{-2} M $KClO_4$ (dashed line) and a series of formal MOP concentrations ranging from 5 x 10^{-5} M to 1.0 x 10^{-3} M. At potential below -0.70 V, MOP curves for all the concentrations merges with the electrolyte curve indicating that an electrode-electrolyte interface free of specifically

adsorbed pyridine derivative. The charge density data of MOP on Au(111) supports the interpretation of DC curves of MOP at electrolyte pH = $pK_{a,\ MOPH+}$. All the MOP curves show an inflection centred at approximately -0.55 V, followed by a linear region that attributed to state I adsorption. An inflection centred at ca. 0.10 V is follwed by another linear region at the positive potentials, which corresponds to state II adsorption. The state I exhibit lower charge density due to lower coverage of the MOP molecules with horizontal orientation on the electrode surfaces. The region with comparatively large charge density reveals that along the state II, high packing density of MOP happens due to a vertical orientation on the electrode surface.

Even though the charge density curves of DMAP (red solid line) and MOP (black solid line) are extremely similar, a subtle difference can be observed between the two by differentiating the σ_m-E plots (inset Figure 3.2). The differential capacity curves obtained from charge density data shows that MOP exhibits more pronounced phase transition compared to DMAP. The potential window corresponding to state I and state II adsorption is significantly larger for MOP compared to DMAP. The narrow potential window of state II adsorption for DMAP can be attributed to competitive adsorption of hydroxide ions at positive potentials.[7] However, the same rationale does not fit for explaining DMAP state I adsorption since OH^- adsorption has minimal influence at lower applied potentials.

3.3.3 Esin-Markov Coefficient

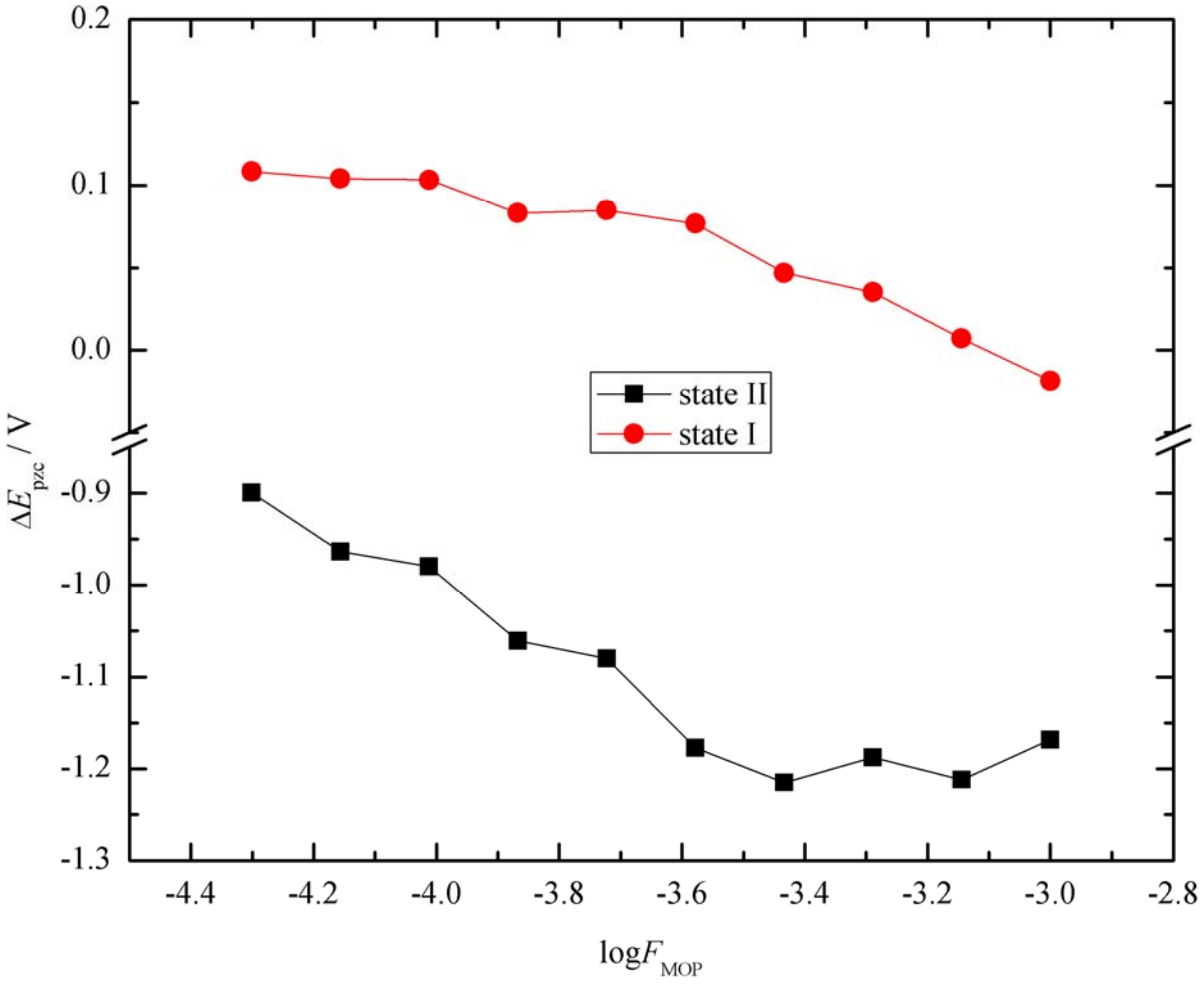

Figure 3.3. Esin-Markov plots showing the potential of zero charge of the Au(111) electrode as a function of the formal MOP concentration for state I (♦) and state II (■) adsorption at $pH_{electrolyte} = pK_{a,\ MOPH+}$.

More information regarding the chemical state of the adsorbed molecule can be obtained from Esin-Markov coefficient ($\partial \Delta E_{pzc}/\partial \mu$). Here, $\Delta E_{pzc} = E_{pzc} - E^{0}_{pzc}$, is the difference in the potential of zero charge (*pzc*) of the electrode with and without adsorbing molecule present in the electrolyte and μ is the chemical potential of the adsorbing species. The *pzc* was determined from the charge density plot (Figure 3.3) by extrapolating the potential corresponding to a given state of adsorption to σ_m = 0 ηC.cm^{-2}. A weakly negative Esin-Markov coefficient is expected when neutral molecules like pyridine derivatives coordinates

through their π system and the shift in the *pzc* will be more negative upon the adsorption of molecule horizontally. Meanwhile, a positive slope for the ΔE_{pzc} versus μ represents adsorption of protonated pyridine derivatives.[8,9] The ΔE_{pzc} for the state I adsorption of MOP is very small and weakly negative dependence on formal concentration, which supports the claim that state I belongs to horizontal adsorption of MOP. And it is evident from the ΔE_{pzc} for state II, which shifted negative by over 1.0 V and shows much stronger concentration dependence, that state II represents vertical adsorption of MOP. In addition, Figure 3.3 clearly depicts that MOP, like DMAP, adsorbs to the Au(111) surface as the neutral molecule at pH = pK_a and the molecular adsorption geometry is absolutely determined by the electrical state of the metal.

3.3.4 Gibbs Surface Excess

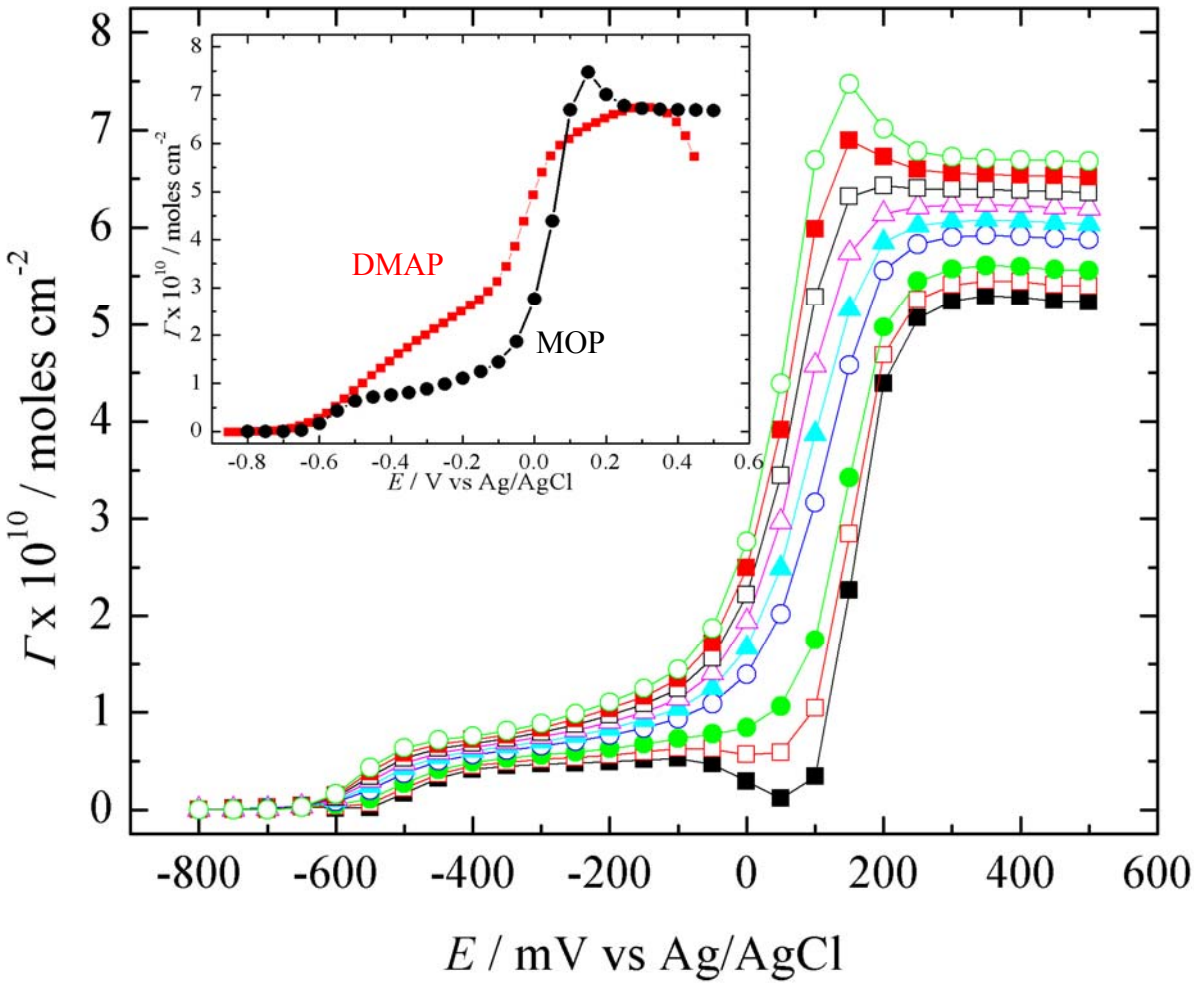

Figure 3.4. Gibbs surface excess for Au(111) at $pH_{electrolyte} = pK_{a,\ MOPH+}$ for the different formal concentrations of MOP (5×10^{-5} M (■), 7×10^{-5} M (□), 1.0×10^{-4} M (●), 1.9×10^{-4} M (○), 2.6×10^{-4} M (▲), 3.7×10^{-4} M(△), 5.1×10^{-4} M (□), 7.2×10^{-4} M (■) and 1.0×10^{-3} M (○)). The inset figure shows comparison of the Gibss excess of MOP (black) and DMAP (red) at same concentration (1.0×10^{-3} M).

As discussed in Chapter 2, the Gibbs surface excess can be obtained from the charge density data through back integration technique. A qualitative examination of the plot shows a two-state adsorption of MOP with a region (-0.50 V < $E_{Ag/AgCl}$ < 0.0 V) of low coverage and a region ($E_{Ag/AgCl}$ > 0.15 V) of higher coverage. The Gibbs surface excess plot quantifies the adsorbed MOP molecules at the two stages of adsorption (Figure 3.4). The lowest and highest MOP concentration curves show anomalous shape at the phase transition region. The former

curve shows a drop in the surface excess and the later curve shows a peak at the transition region (0.0 to 0.1 V). These features of curves at higher and lower concentration would seem to be an artefact. It is assumed that an artefact during the numerical differentiation of the fitted polynomials used to evaluate the partial derivatives in equation 2.17 is the reason for the above mentioned anomalous curves. The limiting surface excesses for the state I and II are rather apparent and are approximately 1.0 x 10^{-10} moles.cm^{-2} and 6.7 x 10^{-10} moles.cm^{-2}. These values are in agreement with the reported values for the π-bonded (state I) and N-bonded (state II) adsorption of pyridine and its derivatives on Au(111) electrodes.[2-3, 10]

A comparative plot of the Gibbs surface excess of MOP and DMAP is included in the inset of Figure 3.4. Even through the state II coverages are essentially identical, state I coverage of MOP is two to three times smaller than state I coverage of DMAP. The expected coverage based on the geometric footprints for pyridine, DMAP and MOP in state I are 1.5 x 10^{-10} moles.cm^{-2}, 1.2 x 10^{-10} moles.cm^{-2} and 1.0 x 10^{-10} moles.cm^{-2} respectively. The measured values for the maximum state I coverage for pyridine, DMAP and MOP are 1.4 x 10^{-10} moles.cm^{-2}, 2.9 x 10^{-10} moles.cm^{-2} and 1.1 x 10^{-10} moles.cm^{-2} respectively.[4, 6] The discrepancy between expected and measured results can be attributed to the remarkable dependence of pyridine derivatives on surface crystallography. Hoon-Khosla *et al*. reported that defects on Au(111) surfaces result in N-bonded Py adsorption.[11] Since the DC measurements of MOP on Au(polycrystalline) electrode shows state II adsorption only (Figure 3.1 (a)), additional MOP molecules bonded through N-sites onto the defective sites on Au(111) surface will also contribute to the measured surface excess. Hence, the relative degree of miscut in the Au(111) electrodes used in the three studies has dramatic impact on the measured state I coverage.

3.3.5 Gibbs Energy of Adsorption

The affinity of ligand molecules to bind on metal's crystalline surface can be measured in terms of Gibbs energy of adsorption. The surface free energy of adsorption of the model molecule can be deduced from the available thermodynamic data by choosing an appropriate adsorption model. The generic Langmuir model for adsorption of a model molecule, Py, requires consideration of the free base species and the number of sites, *S*, available for adsorption

$$\mathrm{Py(aq)} + S \rightleftharpoons \mathrm{Py(ads)} \qquad K_{\mathrm{ads}}$$

$$K_{ads} = \frac{\Gamma_{Py}}{S \cdot a_{Py}(aq)} \qquad \text{Eq 3.1}$$

With the assumption that maximum monolayer coverage (Γ_{max}) occurs when the Py molecules occupy every possible adsorption site, equation 3.1 can be written in terms of surface excess

$$K_{ads} = \frac{\left(\Gamma_{Py} / \left(\Gamma_{\max} - \Gamma_{Py}\right)\right)}{a_{Py}(aq)} = \frac{\left(\Gamma_{Py} / \left(\Gamma_{\max} - \Gamma_{Py}\right)\right)}{\chi_{Py} / \chi^{o}_{Py}} \qquad \text{Eq 3.2}$$

In the aqueous state, at pH = $pK_{a,Py}$, the model molecule will be in equilibrium with its conjugate acid species, the acid dissociation equilibrium will influence the adsorption. Therefore, the expression for the mole fraction of base form in equation 3.2 can be expressed in terms of formal mole fraction

$$\frac{\Gamma_{Py}}{\left(\Gamma_{\max} - \Gamma_{Py}\right)} = \frac{\chi_F}{\chi^{o}_{Py}\left(1 + \beta\chi_H\right)} K_{ads} \qquad \text{Eq 3.3}$$

where the expression for β is provided in Section 2.5. As indicated before, the surface excess in equation 3.3 is numerically analysed through integration and differentiation steps (refer Figure 2.6). Such mathematical treatment to obtain the surface excess can generate

significantly large error. And the K_{ads} determined from the equation 3.3 will have larger uncertainty due to error propagation.

An equivalent expression for the Langmuir adsorption isotherm in terms of surface pressure can be derived to obtain a much more reliable result. Equation 2.17 can be rearranged as the surface pressure in terms of the surface excess

$$\Pi = RT\int \frac{\Gamma_{Py}}{\chi_F} d\chi_F \qquad \text{Eq 3.4}$$

By combining equations 3.3 and 3.4, the expression for surface excess can be written as

$$\Pi = RT\Gamma_{\max} \ln\left[K_{ads}\chi_F + \chi_{Py}^{o}\left(1+\beta\chi_H\right)\right] \qquad \text{Eq 3.5}$$

And the above equation can be linearized into

$$\exp\left[\frac{\Pi}{RT\Gamma_{\max}}\right] - \chi_{Py}^{o}\left(1+\beta\chi_H\right) = K_{ads}\chi_F \qquad \text{Eq 3.6}$$

When the pH = pK_a, and all standard states equate to unit mole fraction, $\chi_{Py}^{0}(1+\beta\chi_H)$ equals to 2 and a plot of $\exp\left[\frac{\Pi}{RT\Gamma_{\max}}\right]$ *versus* χ_F has a slope of K_{ads}.

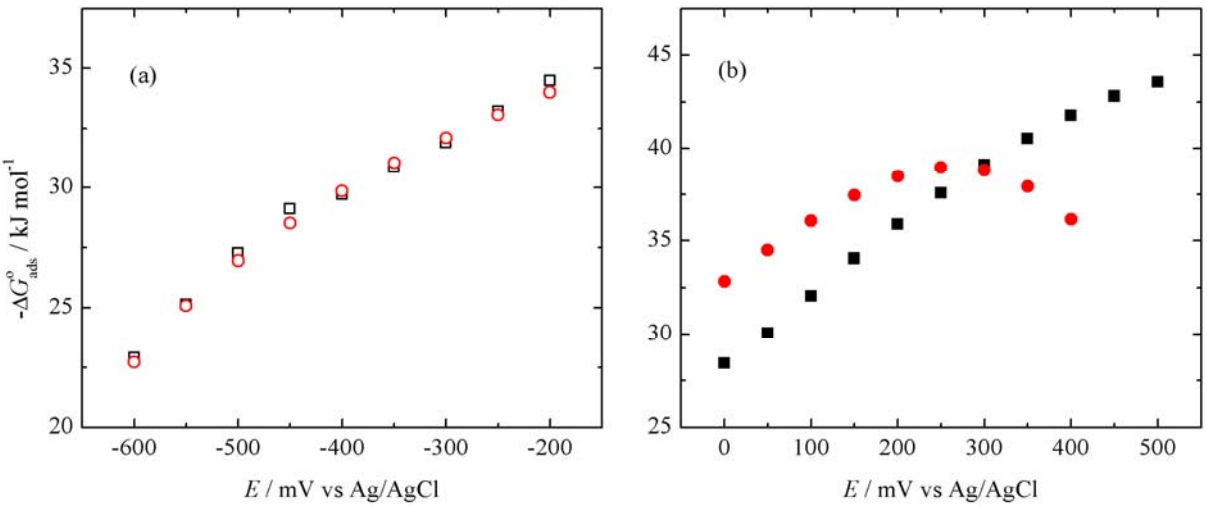

Figure 3.5. Gibbs energy of adsorption as a function of potential for MOP (black) and DMAP (red) for the (a) state I and (b) state II at $pH_{electrolyte} = pK_a$ of the corresponding species.

From the equation 3.6, equilibrium constant can be extracted and then standard free energies of adsorption, ΔG^{o}_{ads}, for the state I and II adsorption can be calculated. Figure 3.5 clearly depicts that MOP and DMAP show almost identical adsorption energy for state I. Whereas in state II, the DMAP shows superior adsorption energy over MOP, which implies DMAP can strongly bind to Au surface via pyridinic N. At larger positive potentials, MOP shows higher adsorption energy than DMAP. However, considering the fact that DMAP suffers from competitive adsorption of hydroxide ions at pH = pK_a, $_{DMAPH^+}$ = 9.7 which artificially lowers its surface pressure at positive potentials, DMAP shows stronger adsorption on Au(111) compared to MOP on a rational scale. In brief, it evident from the processed electrochemical data, that DMAP shows higher affinity and coverage on Au(111) compared to MOP. Moreover, this conclusion supports the findings of Gandubert and Lennox that the Lewis base character of the Py-derivative plays a significant role in NP stabilization and phase-transfer.[12]

3.4 Summary and Conclusions

The pH-dependent adsorption of MOP on Au (111) has been evaluated using electrochemical techniques and various thermodynamic parameters including surfaces excess and Gibss energy of adsorption for MOP were extracted. The features of MOP adsorption has been compared and contrasted to the DMAP adsorption. The electrochemical data indicates that at pH equals to $pK_{a,\ MOP}$, only unprotonated species of MOP adsorbs on Au (111), and there is a shift in the orientation of adsorbed MOP from π-bonded to N-bonded as a function of surface potential. In total, the adsorption behaviour of MOP is analogous to DMAP, although the adsorption energy of MOP in vertical configuration, obtained from Langmuir adsorption isotherm, is lower than that of DMAP on Au(111) surface. Hence, it is evident from the above electrochemical evaluation that, MOP can form a high density molecular film via vertical orientation, on Au (111) facets at moderately acidic and neutral pH, which is a

prerequisite for stabilizing anisotropic growth of NPs along {111}. The comparatively weak adsorption of MOP with respect to DMAP indicates the easy ligand exchange ability of MOP from Au(111) at certain reaction conditions. In summary, the electrochemical investigation of MOP adsorption on Au (111) concludes that MOP is a suitable candidate to be used as ligand to synthesis NPs at moderately acidic to neutral pH conditions. And the available electrochemical adsorption data is useful in manipulating the reaction conditions for MOP assisted, shape/size controlled NP synthesis.

References

1. Parsons, R., The electrical double layer: recent experimental and theoretical developments. *Chemical Reviews* **1990,** *90* (5), 813-826.
2. Lipkowski, J.; Stolberg, L., Adsorption of molecules at metal electrodes. Lipkowski, J.; Ross, P. N., Eds. VCH: 1992; pp 171-238.
3. Barlow, B. C.; Burgess, I. J., Electrochemical Evaluation of 4-(Dimethylamino)pyridine Adsorption on Polycrystalline Gold. *Langmuir* **2007,** *23* (3), 1555-1563.
4. Vivek, J. P.; Burgess, I. J., Crystallographic dependence of 4-dimethylaminopyridine electrosorption on gold. *Electrochimica Acta* **2013,** *88* (0), 688-696.
5. Perrin, D. D., Tables. In *Ionisation Constants of Inorganic Acids and Bases in Aqueous Solution (Second Edition)*, Perrin, D. D., Ed. Pergamon: 1982; pp 1-138.
6. Stolberg, L.; Morin, S.; Lipkowski, J.; Irish, D. E., Adsorption of pyridine at the Au(111)-solution interface. *Journal of Electroanalytical Chemistry and Interfacial Electrochemistry* **1991,** *307* (1–2), 241-262.
7. Chen, A.; Lipkowski, J., Electrochemical and Spectroscopic Studies of Hydroxide Adsorption at the Au(111) Electrode. *The Journal of Physical Chemistry B* **1999,** *103* (4), 682-691.
8. Damaskin, B.; Frumkin, A.; Chizhov, A., Generalized model of the surface layer for the case of adsorption of organic molecules on the electrode. *Journal of Electroanalytical Chemistry and Interfacial Electrochemistry* **1970,** *28* (1), 93-104.
9. Blomgren, E.; Bockris, J. O. M., The Adsorption of Aromatic Amines at the Interface: Mercury-Aqueous Acid Solution. *The Journal of Physical Chemistry* **1959,** *63* (9), 1475-1484.
10. Chen, A.; Yang, D.; Lipkowski, J., Electrochemical and FTIR studies of 4-cyanopyridine adsorption at the gold(111) | solution interface. *Journal of Electroanalytical Chemistry* **1999,** *475* (2), 130-138.
11. Hoon-Khosla, M.; Fawcett, W. R.; Chen, A.; Lipkowski, J.; Pettinger, B., A SNIFTIRS study of the adsorption of pyridine at the Au(111) electrode–solution interface. *Electrochimica Acta* **1999,** *45* (4–5), 611-621.
12. Gandubert, V. J.; Lennox, R. B., Assessment of 4-(Dimethylamino)pyridine as a Capping Agent for Gold Nanoparticles. *Langmuir* **2005,** *21* (14), 6532-6539.

Chapter 4

Surface-Enhanced Infrared Studies of 4-Methoxypyridine Adsorption on Polycrystalline Gold Surface

4.1 Introduction

During electrochemical reactions the electrode-electrolyte interface is enriched by complex processes including accumulation and selective adsorption of ions, solvation/desolvation of ions and reorganisation of solvent molecules, and charge transfer between the electrode and electrolyte.[1] Molecular level detailing of the processes at the electrode-electrolyte interface is a challenge. Some of the popular *ex-situ* techniques employed for characterising electrode-electrolyte interfaces are X-ray photoelectron spectroscopy (XPS), Low energy ion scattering (LEIS), Low energy electron diffraction (LEED), X-ray absorption spectroscopy (XAS) including grazing-incident XAS, scanning transmission X-ray microscopy (STXM), and transmission electron microscopy.[2,3,4] The major drawback of *ex-situ* techniques is the fact that breaking the interface during characterisation may alter the electrode surface as well as the adsorbed molecules/ions. Meanwhile, effectively characterising the interface with *in-situ* techniques requires probes such as sharp tips, electrons, or photons that are capable of generating information solely from the interface without the interference from bulk solid or liquid. Moreover, the dynamic nature of the interface due to Brownian motion and other thermal disturbances, as well as very low analyte concentration at the interface are the major challenges for *in-situ* characterization of interfaces.[5] Fortunately, technical advancement has made many *in-situ* techniques feasible to study the electrode-electrolyte interface, including electrochemical scanning tunnelling microscopy (EC-STM), surface-enhanced vibrational spectroscopy, surface X-ray diffraction/scattering, surface X-ray absorption (near-edge and extended fine structure), and environmental transmission electron microscopy (E-TEM). Among these

techniques, surface-enhanced vibrational spectroscopies are quite popular.[6] The interactions of photon-matter and electron-matter are faster than Brownian motion at the solid-liquid interface. Moreover, these techniques make use of surface plasmons to probe surface processes, which makes them surface sensitive. Moreover, the surface enhancement magnifies the weak signals due to low analyte concentration.

This thesis chapter involves surface-enhanced infrared absoprtion spectroscopy (SEIRAS) studies that provide a detailed molecular picture of the orientation of MOP molecules on polycrystalline Au surfaces. Chapter 2 provides an elaborate description of the experimental procedure. The results and interpretation of potential dependent IR spectra of MOP in adsorbed state are discussed in the following sections.

4.2 Experimental

4.2.1 Reagents, Solutions and Electrode Materials

All chemicals including 4-methoxypyridine (97%), potassium perchlorate (+99%) and perchloric acid (70%) were purchased from Sigma-Aldrich. $KClO_4$ was used after double recrystallization from Milli-Q ($\geq$18.2 MΩ cm^{-1}) water and all other chemicals were used as received. 4-Methoxypyridinium perchlorate (MOP.$HClO_4$) was obtained by the dropwise addition of neat MOP into concentrated $HClO_4$. The white-coloured, needle-like MOP.$HClO_4$ crystals were dissolved in Milli-Q water and precipitated by addition of diethyl ether. The pH of the electrolyte solution was adjusted to the desired value using either dilute KOH or dilute $HClO_4$. A spiking solution of MOP was made with the required ratio of MOP to MOP.$HClO_4$ to maintain a constant electrolyte solution pH.

4.2.2 Transmission and ATR-SEIRAS Measurements

The transmission spectra of MOP were measured from drop casted thin films of neat MOP on a clean CaF_2 window. The MOP.$HClO_4$ transmission spectra were collected using

KBr pellets. All ATR-SEIRAS measurements were performed using a glass spectroelectrochemical cell built in-house. A 25 mm diameter silicon hemisphere (Harrick) coated with gold was used as the working electrode. The silicon hemisphere was polished with 3 μm as well as 0.5 μm diamond polishing suspensions and then cleaned ultrasonically with ethanol (95%) and Milli-Q water. Prior to the gold deposition, the silicon hemisphere face was treated with NH_4F (40 V%) to remove the oxide layer. The gold layer on the silicon hemisphere was achieved by using a Denton Vacuum Desk IV cold sputter and a deposition rate of ~ 0.02 $nm.sec^{-1}$ for 25 minutes to reach an optimum film thickness of ~30 nm. The formal concentration of MOP/H^+ in all experiments was $1x10^{-4}$ M. An externally connected Ag/AgCl wire in saturated KCl served as the reference electrode. The supporting electrolyte solution ($5x10^{-2}$ M $KClO_4$ for all experiments) was de-oxygenated for 30 minutes before the measurements, and an argon blanket was maintained inside the cell throughout the experiment. The potential of the Au-film serving as both the SEIRAS active substrate and the working electrode was controlled using a HEKA PG 590 potentiostat. Prior to the addition of MOP/H^+, the Au layer on the silicon hemisphere was electrochemically polished in $5x10^{-2}$ M $KClO_4$ by cycling the potential between the open circuit potential (OCP) and 1.2 V. An in-house developed LabVIEW program was used to control both the Bruker Vertex 70 FT-IR spectrometer and the potentiostat while performing the potential dependent SEIRAS experiments. The incident angle of the IR beam was 70^o and all spectra were collected with 4 cm^{-1} resolution between 4000 cm^{-1} to 400 cm^{-1}. Each spectrum was the result of the co-addition of 128 interferograms. Final spectra are reported as relative changes in absorbance, $\Delta Abs = -\log\left(R_E / R_{E_{ref}}\right)$ where R_E and $R_{E_{ref}}$ are the single-beam signals recorded at the reference potential (-0.70 V vs Ag/AgCl) and the sample potential respectively.

4.3 Results and Discussion

4.3.1 IR Spectra of MOP and MOP•$HClO_4$ in Transmission Mode

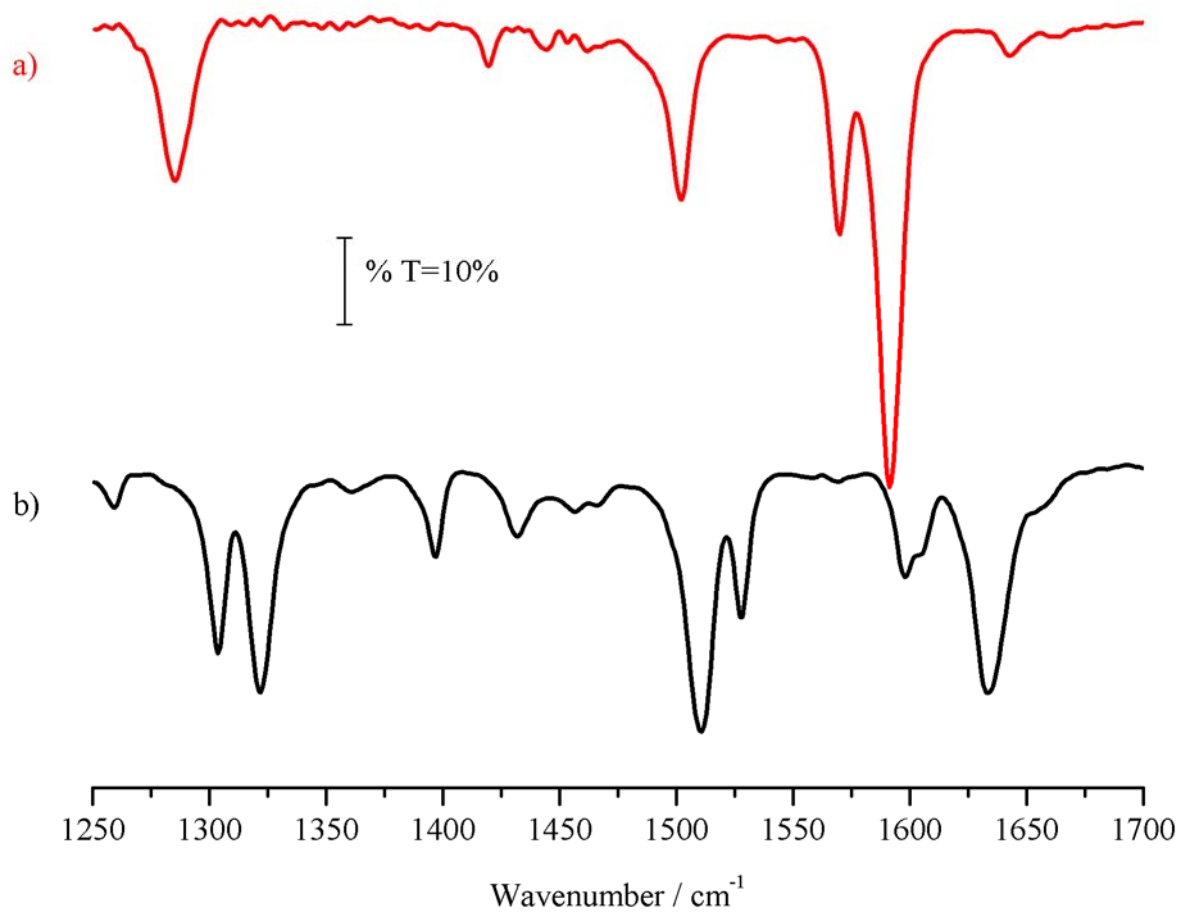

Figure 4.1. Transmission spectra of a) MOP (—) and b) MOP.$HClO_4$ (—).

Infrared spectra of MOP and its conjugate acid were measured in transmission mode to support the SEIRA spectra. The transmission spectrum of MOP and MOP.$HClO_4$ shown in Figure 4.1 are compared with the reported experimental work of Spinner and White.[7] The free base shows an intense band at 1592 cm^{-1} along with four other dominant bands. When the methoxy group lies in the plane of the pyridine ring, MOP has C_s point group symmetry.[8] The transition dipole moment for any normal mode will be either in the molecular plane (A′) or orthogonal to the molecular plane (A′′). The CH_3 scissoring vibration is the only possible A′′ mode in the spectral region of interest and is expected to be weak relative to the ring vibrations of the pyridine group. Gaussian09[9] and the B3LYP density functional with the 6-

311++G basis set is used to generate quantum mechanically calculated MOP IR spectra for the vibrational peak assignment (Table 4.1). Even though the calculated MOP spectrum is in agreement with Spinner and White's interpretations, there is a discrepancy regarding assignment of the strong absorption at ~ 1500 cm^{-1}. Cook *et al*. attributes this peak solely to a single ring vibration (υ19a) whereas our calculations show this to be a composite of closely overlapping signals arising from skeletal ring vibrations as well as the aforementioned A´´ CH_3 scissoring vibration.[10] Another striking feature of the calculated spectrum is, the larger magnitude of the transition dipole moment for the υ18a (a lower frequency A´ vibration), which dominates the calculated spectrum. All together, the experimental, literature, and calculated transmission spectra indicates that between 1250 cm^{-1} and 1700 cm^{-1} MOP displays four, medium to strong A´ bands arising from ring skeletal vibrations and ring vibrations coupled to the atomic displacements of the methoxy group. In the case of MOP.$HClO_4$, protonation leads to both a blue shift in the spectral features compared to its free base analogue and an increase in the number of bands. Similar shifts to higher frequencies for the ring vibration modes has been reported in the case of conjugated acids of pyridine and its derivatives, due to delocalization of the positive charge.[7, 10-11] Unfortunately, the explanation for intensity change on the vibrational frequencies due to protonation of the substituent is more complicated. In the case of 4-MOP•HCl, the frequencies of the symmetric and asymmetric COC bands are lowered and raised respectively upon protonation of methoxypyridine making it difficult to unambiguously assign all the bands appearing in Figure 4.1 (b). In addition, the quantum mechanical calculations are in poor agreement with the experimental data below 1400 cm^{-1} where the asymmetric COC stretches are expected. Therefore, the report by Spinner and White has been used primarily to assign the peaks reported in Table 4.1 although the DFT results were used to help interpret the poorly separated peaks between 1500 cm^{-1} and 1550 cm^{-1}. Similar to MOP spectra, the most

prominent vibrational peaks in the transmission spectrum of the conjugate acid are assigned to A´ modes.

Table 4.1. Assignment of transmission infrared vibrational bands for MOP and its conjugate acid.

Methoxypridine				
Description	Symmetry class	Measured	Literature[a]	Calculated[b]
Ring vibration (8a)	A´	1591	1597,s	1593
Ring vibration (8b)	A´	1570	1574,m	1562
Ring vibration (19a)	A´		1507,m	1504
CH_3 bend	A´´		n/a	1500
Ring vibration (18a)	A´	1501	n/a	1493
CH_3 bend#1	A´	1465	1465,w	n/a
CH_3 bend#2	A´	1454	1445,w	1455
Ring vibration (19b)	A´	1420	1423,w	1422
COC (asym. stretch)	A´	1286	1289,s	1269
Methoxypridinium perchlorate				
Ring vibration (8a)	A´	1633	1635,s	1623
Ring vibration (8b)	A´	1600	1600,m	1600

s = strong; m = medium; w = weak; sh = shoulder; n/a = not observed.

[a] Assignments are made on both the basis of reference.7. Spinner, E.; White, J. C. B., 602. The vibration spectra of the cations of methoxypyridines. *Journal of the Chemical Society (Resumed)* **1962,** (0), 3115-3118.

[b] Calculated frequencies have been multiplied by a factor of 0.985 to account for harmonic approximation.

Ring vibration (19b)	A´	1528	1529,m	1538
Ring vibration (18a)	A´			1528
CH3 bend	A´´	1510	1512,s	1504
Ring vibration (19a)	A´			1500
CH3 bend	A´	1457	1459,w	n/a
CH3 bend#2	A´	1432	1433,w	1468
Unassigned	A´	1398	1398,m	n/a
COC (asym. stretch)	A´	1322	1322,s	n/a
COC (asym. stretch)	A´	1304	1304,s	n/a
Ring vibration (9b) + COC a-st.	A´	1259	1259,w	1251

4.3.2 SEIRA Spectra at the Open-Circuit Potential

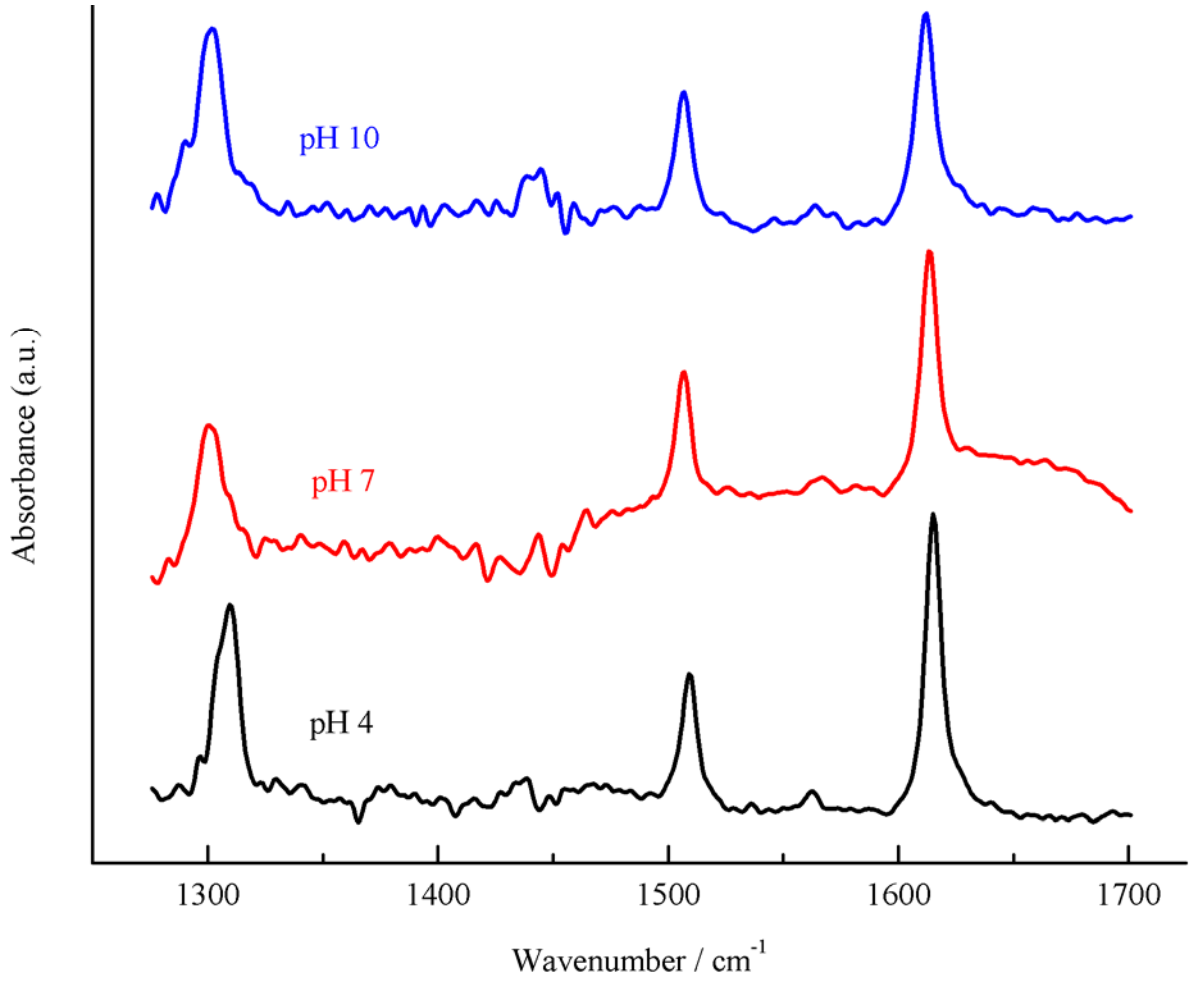

Figure 4.2. SEIRAS spectra of MOP/H^+ at ocp at pH 10 (—), pH 7 (—) and pH 4(—).

The SEIRA spectra at open circuit potential (ocp ~ +0.1 V) for three different pH values are collected and expressed as relative absorptions (Figure 4.2). The reference spectra were collected with MOP free electrolyte at the corresponding pH. Irrespective of electrolyte acidity, all three spectra display three strong upward bands at ~ 1310 cm^{-1}, 1510 cm^{-1} and 1615 cm^{-1}. The strong MOP signal at higher wave number is not superimposed on a negative going feature associated with displaced water molecules from the Au surface and the following hypothesis explains this spectral feature. The reference spectra are collected at a potential closer to the *pzc* for $5x10^{-4}$ M $KClO_4$. Randomly organized water molecules on uncharged polycrystalline gold have been reported[12] and would only be weakly SEIRAS active.

In Chapter 3, electrochemical studies of MOP on Au (111) demonstrated that, like other pyridine analogues, MOP adsorbs on the gold surface as the neutral molecule at pH >> pK_a.[13] The IR spectra in Figure 4.2 support this statement as the spectrum certainly more closely resembles the transmission spectrum of MOP than the spectrum of MOP•$HClO_4$. At low pH, the ionic equilibrium shifts in favour of the pyridinium ion and thus it becomes the principal species present in solution. Though $MOPH^+$ is assumed to replace MOP and exhibit its corresponding bands, the similarity of all three spectra in Figure 4.2 implies that $MOPH^+$ does not adsorb on Au at ocp and must have weaker adsorption energy.

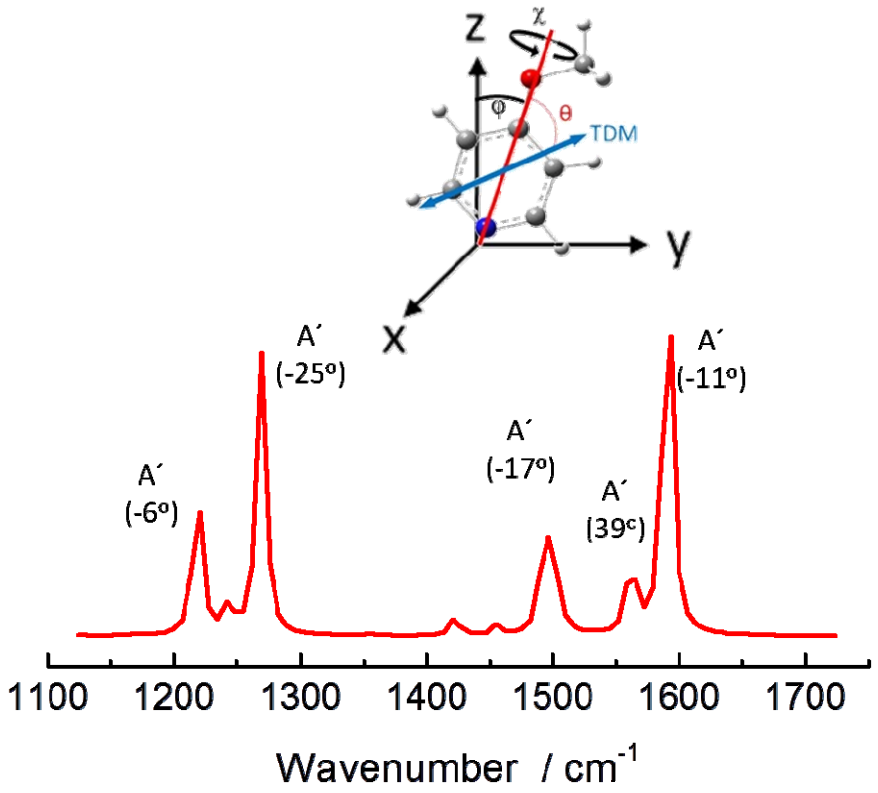

Figure 4.3. DFT-calculated spectrum for MOP as well as a Cartesian coordinate system, (φ) the tilt angle between the gold surface's perpendicular and the principal molecular axis , (χ) rotation around the molecular axis and (θ) the angle between the TDM of any particular A´ vibration and the molecular axis.

Unlike the calculated spectra, the appearance of discrete peaks rather than closely paired peaks at ~1625 cm^{-1}, ~1500 cm^{-1} and ~1300 cm^{-1} is most telling. Nevertheless, there are

noticeable differences in the peak positions of ocp SEIRAS spectrum at pH 10 compared to the MOP transmission spectrum in Figure 4.1 (a), especially the blue shift in the 1625 cm^{-1} as well as the 1310 cm^{-1} peak. In addition, the weak adsorption bands associated with the methyl bending modes are missing as is the strong ring vibration assigned as υ8b. The orientations of the adsorbed molecules are related to the missing bands, which can be explained as follows. As discussed in the previous chapters, two states of adsorption are characteristic features of pyridine and its para substituted derivatives. To reiterate, during horizontal adsorption the heterocyclic's π electron system interacts with the metal and in vertical adsorption, the lone pair of electrons on the ring nitrogen forms a σ-type bond with the Au surface. Upon horizontal adsorption of MOP (or its conjugate acid, $MOPH^+$), the surface selection rules for SEIRAS[14] would render all the A′ modes inactive and only the A′′ methyl bending mode would be observed. Since all the spectra in Figure 4.2 display strong three A′ bands, it is evident that MOP/H^+ is vertically oriented on the surface at the ocp.

The parent pyridine molecule shows two types of in-plane ring vibrations, A_1 and B_1. Those vibrations with A_1 symmetry class have their transition dipole moment (TDM) collinear with the principal molecular axis and those with B_1 symmetry class have TDMs orthogonal to the C_2 axis. Hoon-Khosla *et al* reported A_1 and B_1 intensities of adsorbed pyridine and were able to determine that a) the plane of vertically oriented pyridine is tilted with respect to the electrode surface and b) there exists some contribution from N-bonded pyridine on defect sites on Au(111) surfaces at potentials where π-bonded configuration is favourable.[15] Based on the intrinsic intensities of the orthogonal A_1 and B_1 modes for the free molecule, Osawa described a comparatively trivial method for determining the orientation of pyridine from SEIRAS measurements.[14] The current study of MOP adsorption using SEIRAS adopts the later approach developed by Osawa.

The DFT-calculated spectrum for MOP as well as a Cartesian coordinate system that defines 1) the tilt angle φ between the surface normal (i.e. the Z –axis) and the principal molecular axis 2) rotation, χ, around the molecular axis and 3) the angle θ between the TDM of any particular A′ vibration and the molecular axis are provided in Figure 4.3. The calculated spectrum shows that the three TDMs for the bands at ~1225 (not seen in the experimental spectrum due to Si hemisphere's long wavelength cutoff), ~1500 and ~1600 cm^{-1} is less than 20^{o} from the principal axis, thus the magnitudes of these A′ bands in the SEIRA spectra provide a measure of the orientation of the molecular axis. On the other hand, the TDs of the band at ~1560 cm^{-1} are considerably off-axis. If the molecule adopts a vertical orientation (i.e. its tilt angle approaches 0^{o}) the vibrational modes with TDMs collinear with the molecular axis get enhanced relative to those with larger absolute θ values. This clearly explains the presence of υ8a and the absence of υ8b when analyzing the higher frequency end of the SEIRAS spectra in Figure 4.2. The following assumptions are required in order to precisely extract the molecular orientation from the calculated angles of TDM 1) the magnitude of calculated TDM for the free molecules and adsorbed molecules are the same, and 2) the inherent SEIRAS enhancement factor is frequency independent. Rather than making these assumptions and arguably over interpreting the available data, it can be simply concluded that the SEIRAS results strongly support the vertical adsorption motif based on the observed/missing A′ bands and the absence of the A′′ band.

4.3.3 Potential-Dependent Adsorption on Polycrystalline Gold

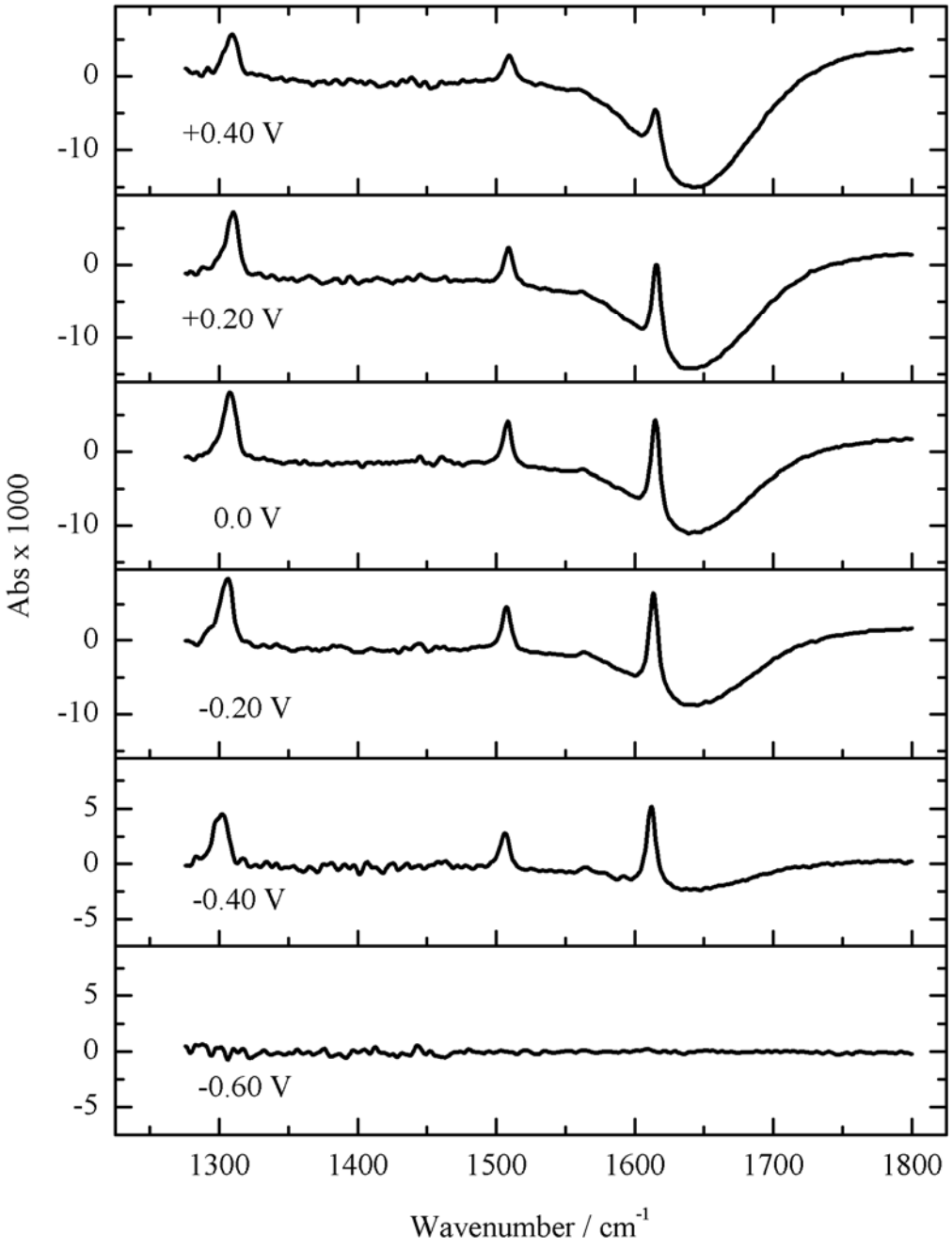

Figure 4.4. Relative changes in absorbance in SEIRAS spectra of MOP mode, at pH 7 as a function of potential. The reference spectrum was collected at -0.70 V.

Performing SEIRAS studies of MOP adsorbed on Au (111) surfaces would be ideal in order to compare the electrochemical data of MOP adsorption on Au (111). Delgado *et al.* reported an electrochemical procedure for generating {111} surface domains on Au films made for SEIRAS studies.[16] However, electrochemical adsorption studies of DMAP shows

that stepped surfaces favour N-bonded adsorption whereas terraces prefer π-bonded adsorption. Thus even a small percentage of defective crystal sites may considerably skew the interpretation of spectra as reported by Hoon-Khoshla *et al*.[15] In order to avoid the discrepancy between thermodynamic and spectroscopic studies Au films without preferential texture are used to perform SEIRAS measurements on MOP adsorption. Moreover, the Au deposition conditions are tightly controlled during every Au film preparation to obtain consistent film textures. DC measurements were performed on several different polycrystalline films in neutral and acidic electrolytes to confirm the consistency of film crystallography. Electrochemical measurements revealed that in both acidic and neutral media, MOP was completely desorbed from the electrode surface at E = -0.70 V. Therefore SEIRA spectra were obtained as a function of potential using the single beam spectrum at E = -0.70 V as the reference. The SEIRA spectra in neutral pH shows the three principal A´ peaks appear starting at E > -0.60 V which first grow in intensity and then weaken at more positive potentials (Figure 4.4). The spectral peaks were examined using the aforementioned TDM analysis and it can be concluded that, in pH 7, the adsorbed molecules have a significant component of the principal molecular axis perpendicular to the metal surface.

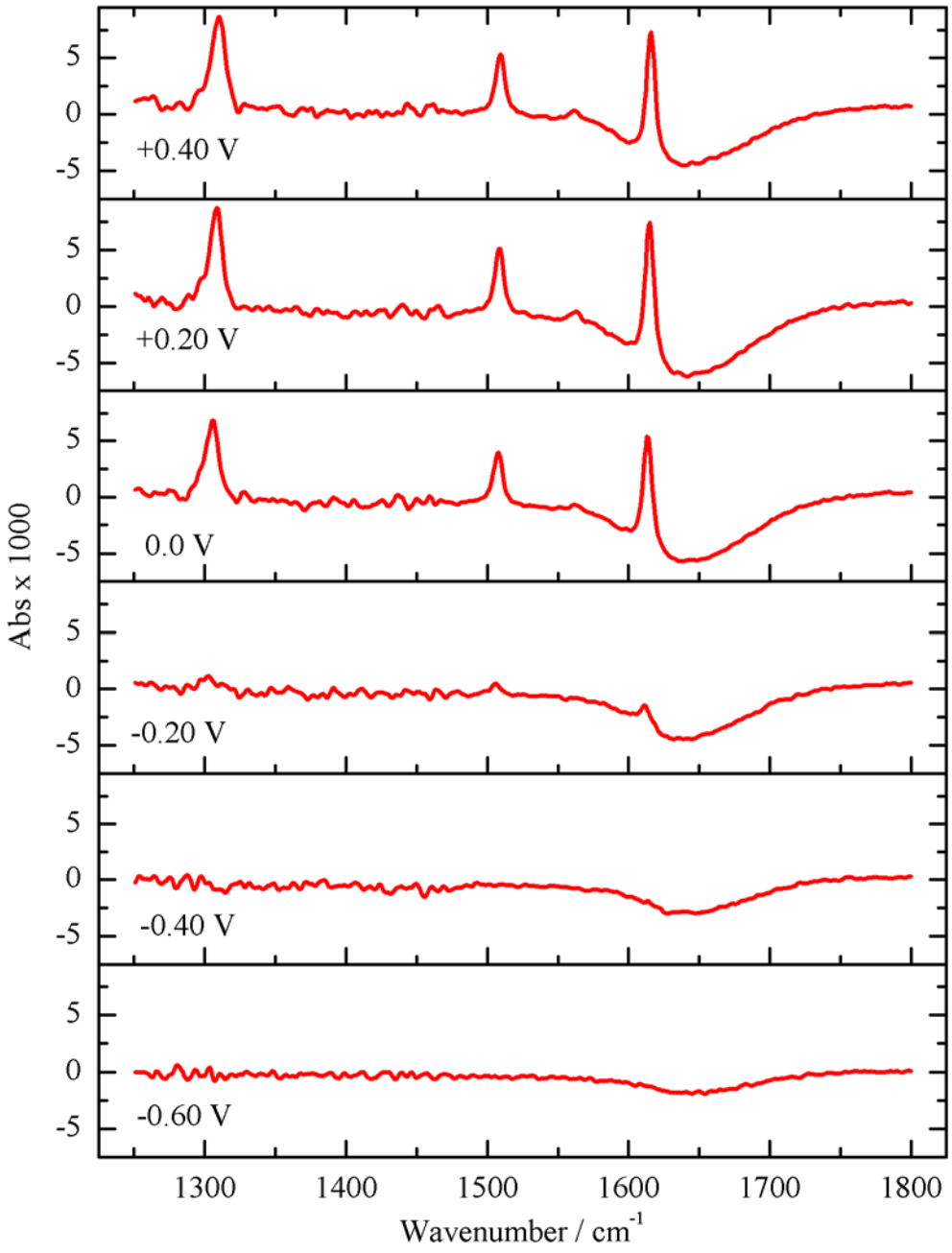

Figure 4.5. Relative changes in absorbance in SEIRAS spectra of MOP mode, at pH 4 as a function of potential. The reference spectrum was collected at -0.70 V.

Figure 4.5 shows an equivalent SEIRAS experiment conducted in pH 4 and the spectra shows the following differences. Primarily, the onset of the IR absorption peaks of MOP in pH 4 shifts to more positive potentials (-0.20 V). At more negative potentials, absence of MOP peaks implies no MOP adsorption but negative bands in the water bending region are

seen at all potentials positive of the reference potential. Surprisingly, the A´ peak intensities do not decrease in magnitude at positive potentials unlike in the case for neutral pH.

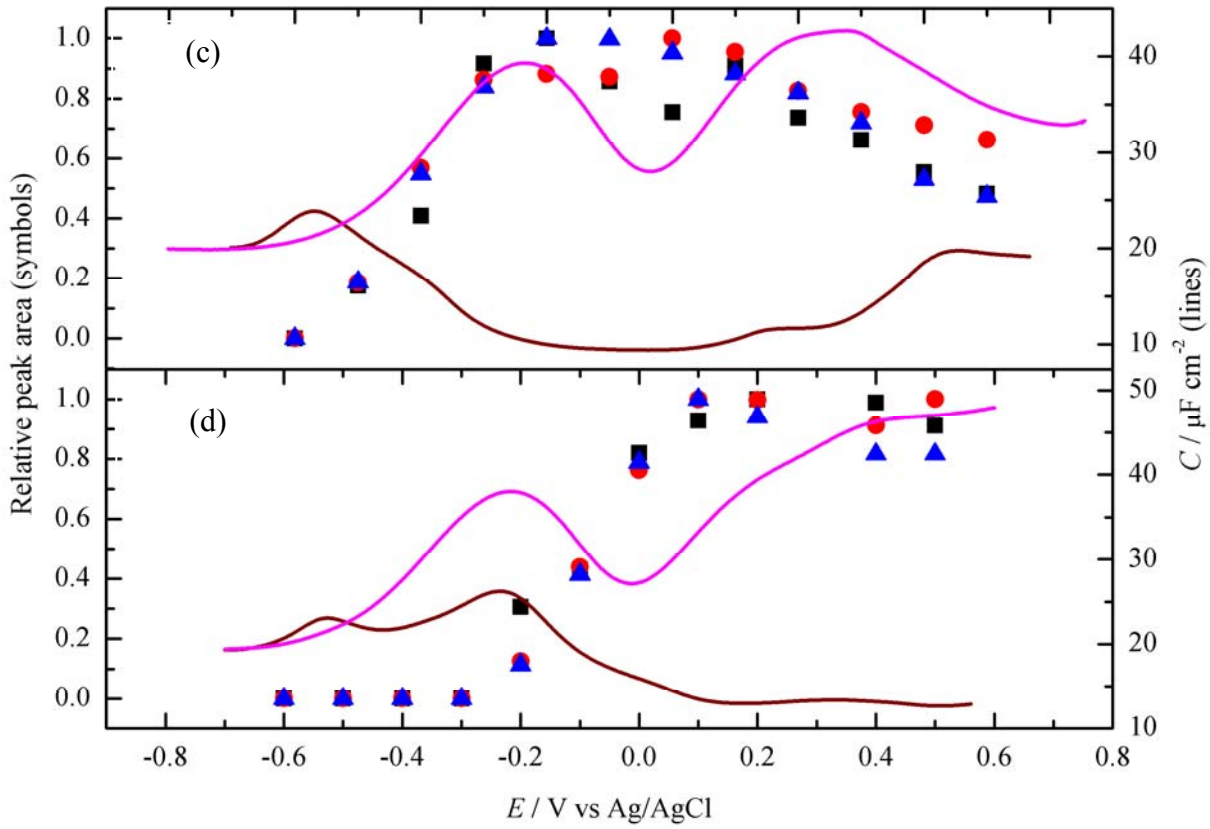

Figure 4.6. Integrated peak areas (left ordinate) for the MOP IR peaks at 1300 cm^{-1} (■), 1500 cm^{-1} (●) and 1625 cm^{-1} (▲) and the differential capacitance curves (right ordinate) for the supporting electrolyte in the absence (—) and presence (─) of 1 x 10^{-4} M MOP (a) in pH 7 (b) in pH 4.

Comparison of integrated peak areas for the two sets of SEIRAS data with the corresponding differential capacity curve is useful in interpreting the IR results (Figure 4.6). The merge of differential capacity curves with and without the addition of MOP supports that any adsorbed species can be completely desorbed at sufficiently negative potentials. The capacity minimum region between -0.40 V < *E* < 0.10 V in neutral electrolyte (Figure 4.6 (a)) shows MOP adsorbs in a single state in this region. All three IR peaks reach a maximum at the same potential as the minimum in the differential capacity curve and the relative

integrated peak areas decrease at roughly the same rate but never completely disappear at more positive potentials. Such spectral behaviour at positive potentials can be interpreted as either partial desorption of MOP from the electrode or reorientation of MOP to form a less compact/thinner inner Helmholtz layer (Figure 4.6). These two possibilities can be differentiated by analysing the vibrational modes of water in this region.

The desorption of MOP can be considered as place exchange with solvent molecules and consequently if MOP was partially desorbed at positive potentials stronger water vibration modes should be present in the spectra. There is a large negative absorbance change in the HOH bending mode (δ (HOH)) at 1645 cm^{-1} and O-H stretching (υ(OH)) at ~3300 cm^{-1}. This observation is in contradiction with the first assumption because partial replacement of MOP by the solvent at positive potentials would be expected to cause a maximum in the water stretching and bending intensities at potentials corresponding to the capacitive minimum. In addition, the structure of the water in the interfacial region influence the positions of υ(OH) and, to a lesser extent δ(HOH), by red shifting the former and blue-shifting the latter with increasing extent of hydrogen bonding.[12] Similar to the structure of water found in adsorbed adenine[17], SDS hemimicelles[18] and adsorbed lipid bilayers[19], water and coadsorbed MOP would be expected to produce a broken hydrogen bonding network of water "multimers". However, the spectral signal from water at positive potentials relates only to the loss of the heavily hydrogen bonded water that covers the electrode surface[12] at the reference potential (E = -0.70 V) and does not provide any formation of hydrogen-bonded multimers indicative of coadsorbed water. Hence, it can be concluded that a conformational change in the adsorbed MOP molecules leads to the decreasing peak areas at higher potentials rather than partially MOP desorption.

UHV studies of pyridine adsorption on various single crystal surfaces suggest the possibility of edge-on adsorption by breaking the C(2)-H bond and coordination via η^2 α-pyridyl.[20] A transition from vertically oriented MOP at 0.0 V to edge-on adsorption at higher potentials requires realignment of the molecular axis with respect to the surface normal. However, based on TDM analysis, such realignment would result in different relative intensity changes in the three observed A′ modes than that of observed spectra. Thus, the possibility of edge-on adsorption can be eliminated. The presence of non-zero MOP adsorption signals at higher positive potentials nullifies a complete transition from vertical to horizontal adsorption since the latter orientation would provide no A′ modes along the surface normal. Therefore, the most plausible interpretation is a potential dependent increased tilt in the ring system toward the gold surface which diminishes the component of all three A′ modes in the Z-direction but in such a way that they retain their relative magnitudes which is in agreement with the data shown in Figure 4.4. STM and IR studies of pyridine adsorption report a similar, tilted adsorption state, intermediate between the vertical and horizontal states.[21] In the case of MOP adsorption, tilting would allow the para substituent to bind with the gold surface via non-bonding electrons on the oxygen atom.

Figure 4.5 provides an equivalent representation of the data at pH 4. The presence of multiple capacity minima (at ~ -0.45 V and $E > 0.0$ V) separated by pseudocapacity peak (-0.25 V) in the DC curves indicates complicated behaviour of MOP adsorption in acidic electrolyte. SEIRA spectra show no MOP signals in the narrow potential region between the adsorption onset peak (-0.60 V) and the pseudocapacitive peak (-0.25 V). However, the presence of negative δ(HOH) bands at all potentials in Figure 4.5 indicates loss of water molecules from the electrode surface and provides indirect proof of solvent displacement by horizontally adsorbed MOP. The integrated peak areas rise as the capacity drops starting at –0.20 V and reach a plateau at potentials matching the limiting capacity ($E \geq +0.10$ V).

Cumulative analysis of Figure 4.6 (b) strongly supports the horizontal to vertical phase transition of MOP in moderately acidic media. In addition, the consistent intensities of the SEIRA spectra at positive potentials in Figure 4.5 supports vertical rather than tilted adsorbed MOP and no spectroscopic evidence of the adsorbed conjugate acid is evident at larger positive potentials.

The relative change in the peak positions with respect to potential can provide addition information about molecular orientation. In neutral pH, all the three peaks show a linear shift until +0.10 V but then shows negative shifts at higher potentials. The tuning rates of the bands at ~1600 cm^{-1} and 1500 cm^{-1} are both ~ 6.5 cm^{-1} V^{-1} which is consistent with previously reported ring vibrations for DMAP [22] and pyridine.[23] Changes in the electric field, charge-redistribution between the adsorbate and the metal, or dipole-coupling caused by the lateral interactions results in potential dependent shifts in the vibrational band positions of molecules adsorbed on electrified interfaces.[24] The surface potential can alter the extent of σ donation between the ring nitrogen and the Au surface, which explains the potential dependence for the ring mode positions in pyridine derivatives. However, the tilted orientation of MOP at higher potentials increasingly develops greater π-bonding character, which attenuates the Stark effect for the A′ ring modes. The asymmetric COC stretch of MOP at ~ 1300 cm^{-1} has more than twice as large a potential dependence (14 cm^{-1} V^{-1}) compared to the higher frequency ring vibrations. It is much stronger compared to the DMAP system where the C-N stretch of the dimethylamino substituent was found to vary only weakly on potential. The dipole coupling effects between the methoxy groups could be a plausible explanation for the stronger Stark effect in the case of MOP whereas the higher degree of steric bulk afforded by the dimethylamino group would mitigate this affect in adsorbed DMAP. SEIRA spectral peaks in acidic pH show monotonic tuning rates over the potential range -0.20 V ≤ E ≤ +0.50 V. The features of potential depended IR spectra such as

an absence of a plateau and the similarity in the Stark shift values are common in pH 7 and pH 4, which provide additional evidence that at positive potentials, MOP shows vertical N-bonded orientation in neutral and moderately acidic pHs.

4.4 Conclusions

A detailed discussion about the potential dependent infrared spectroscopic investigation of 4-methoxypyridine adsorption on polycrystalline Au at neutral and acidic pHs is provided in this chapter. The electrochemical data pertaining to MOP adsorption and documented in Chapter 3 were utilized to help interpret the SEIRAS data. A summary of the findings are as follows: even at conditions where the concentration of $MOPH^+$ dominates over MOP (at pH = 4) in the bulk solution, MOP adsorbs on polycrystalline Au in its free base form. At neutral pH, MOP orients vertically on weakly charged polycrystalline Au surfaces and exhibits an increased tilted orientation at positive potentials. The presence of MOP signals even at higher positive potentials infers that the highest tilt angle of MOP is not enough to obtain a complete horizontal orientation. Meanwhile in acidic conditions, MOP adsorbs horizontally at negative potentials and shifts to vertical configuration at potentials positive of the *pzc* of bare polycrystalline Au. The tilting phenomenon at neutral pH is unique to MOP compared to DMAP; hence, this study also links the effect of pyridine substituent on metal-pyridine interaction.

References

1. Bard, A. J.; Faulkner, L. R., Electrochemical Methods: Fundamentals and Applications, 2nd Edition. Wiley-VCH Verlag GmbH & Co. KGaA: 1980.
2. Lebedev, M. V.; Calvet, W.; Mayer, T.; Jaegermann, W., Photoelectrochemical Processes at n-GaAs(100)/Aqueous HCl Electrolyte Interface: A Synchrotron Photoemission Spectroscopy Study of Emersed Electrodes. *The Journal of Physical Chemistry C* **2014,** *118* (24), 12774-12781.
3. Lin, F.; Markus, I. M.; Nordlund, D.; Weng, T.-C.; Asta, M. D.; Xin, H. L.; Doeff, M. M., Surface reconstruction and chemical evolution of stoichiometric layered cathode materials for lithium-ion batteries. *Nat Commun* **2014,** *5*.
4. Stuhlmann, C.; Park, Z.; Bach, C.; Wandelt, K., An ex-situ study of Cd underpotential deposition on Cu(111). *Electrochimica Acta* **1998,** *44* (6–7), 993-998.
5. Wu, C. H.; Weatherup, R. S.; Salmeron, M. B., Probing electrode/electrolyte interfaces in situ by X-ray spectroscopies: old methods, new tricks. *Physical Chemistry Chemical Physics* **2015,** *17* (45), 30229-30239.
6. Zhang, N.; Schweiss, R.; Zong, Y.; Knoll, W., Electrochemical surface plasmon spectroscopy—Recent developments and applications. *Electrochimica Acta* **2007,** *52* (8), 2869-2875.
7. Spinner, E.; White, J. C. B., 602. The vibration spectra of the cations of methoxypyridines. *Journal of the Chemical Society (Resumed)* **1962,** (0), 3115-3118.
8. Lange, H.; Maultzsch, J.; Meng, W.; Mollenhauer, D.; Paulus, B.; Peica, N.; Schlecht, S.; Thomsen, C., Adsorption Behavior of 4-Methoxypyridine on Gold Nanoparticles. *Langmuir* **2011,** *27* (11), 7258-7264.
9. Frisch, M. J. *Gaussian 09*, Gaussian, Inc.: Wallingford, CT, USA, 2009.
10. Cook, D., Vibrational spectra of pyridinium salts. *Canadian Journal of Chemistry* **1961,** *39* (10), 2009-2024.
11. Kozhevina, L. I.; Rybachenko, V. I., Interpretation of IR spectra of the N-acethyl-4-dimethylaminopyridinium salts. *J Appl Spectrosc* **1999,** *66* (2), 165-170.
12. Ataka, K.-i.; Yotsuyanagi, T.; Osawa, M., Potential-Dependent Reorientation of Water Molecules at an Electrode/Electrolyte Interface Studied by Surface-Enhanced Infrared Absorption Spectroscopy. *The Journal of Physical Chemistry* **1996,** *100* (25), 10664-10672.
13. Unni, B.; Simon, S.; Burgess, I. J., Electrochemical Investigations of 4-Methoxypyridine Adsorption on Au(111) Predict Its Suitability for Stabilizing Au Nanoparticles. *Langmuir* **2015,** *31* (36), 9882-9888.
14. Osawa, M., In-situ Surface-Enhanced Infrared Spectroscopy of the Electrode/Solution Interface. In *Advances in Electrochemical Science and Engineering*, Wiley-VCH Verlag GmbH: 2008; pp 269-314.
15. Hoon-Khosla, M.; Fawcett, W. R.; Chen, A.; Lipkowski, J.; Pettinger, B., A SNIFTIRS study of the adsorption of pyridine at the Au(111) electrode-solution interface. *Electrochim. Acta* **1999,** *45* (4-5), 611-621.
16. Delgado, J. M.; Orts, J. M.; Pérez, J. M.; Rodes, A., Sputtered thin-film gold electrodes for in situ ATR-SEIRAS and SERS studies. *Journal of Electroanalytical Chemistry* **2008,** *617* (2), 130-140.
17. Álvarez-Malmagro, J.; Prieto, F.; Rueda, M.; Rodes, A., In situ Fourier transform infrared reflection absortion spectroscopy study of adenine adsorption on gold electrodes in basic media. *Electrochimica Acta* **2014,** *140*, 476-481.
18. Grossutti, M.; Leitch, J. J.; Seenath, R.; Karaskiewicz, M.; Lipkowski, J., SEIRAS Studies of Water Structure in a Sodium Dodecyl Sulfate Film Adsorbed at a Gold Electrode Surface. *Langmuir* **2015,** *31* (15), 4411-4418.
19. Uchida, T.; Osawa, M.; Lipkowski, J., SEIRAS studies of water structure at the gold electrode surface in the presence of supported lipid bilayer. *Journal of Electroanalytical Chemistry* **2014,** *716*, 112-119.
20. Jones, T. E.; Zuo, C.; Jagodzinski, P. W.; Eberhart, M. E., Molecular Orbital Model for Pyridine/α-Pyridyl Adsorption on Metal Surfaces. *The Journal of Physical Chemistry C* **2007,** *111* (14), 5493-5496.

21. Cai, W.-B.; Wan, L.-J.; Noda, H.; Hibino, Y.; Ataka, K.; Osawa, M., Orientational Phase Transition in a Pyridine Adlayer on Gold(111) in Aqueous Solution Studied by in Situ Infrared Spectroscopy and Scanning Tunneling Microscopy. *Langmuir* **1998,** *14* (24), 6992-6998.
22. Rosendahl, S. M.; Danger, B. R.; Vivek, J. P.; Burgess, I. J., Surface Enhanced Infrared Absorption Spectroscopy Studies of DMAP Adsorption on Gold Surfaces. *Langmuir* **2009,** *25* (4), 2241-2247.
23. Ikezawa, Y.; Sawatari, T.; Toriba, K., In situ FTIR study of pyridine adsorbed on a polycrystalline gold electrode. *Electrochim. Acta* **1998,** *43* (21-22), 3297-3301.
24. Nichols, R. J., IR Spectroscopy of Molecules at Metal Electrodes In *Adsorption of molecules at metal electrodes*, Lipkowski, J.; Ross, P. N., Eds. VCH: New York, 1992.

Chapter 5

Summary and Conclusions

5.1 Summary

This thesis has addressed a major challenge persisting in synthesizing anisotropic NPs: the systematic screening and evaluation of the capping agents. Even though a myriad of procedures for anisotropic NP synthesis is available in the current literature, the working mechanism of capping agents is still largely poorly defined. To reiterate, many hypothetical mechanisms have been proposed that attribute the formation of anisotropic nanoparticle growth to the role of the capping agent. These are usually made without scientific analysis but rather by post-synthesis evaluation of the NP shape. The lack of experimental techniques to directly measure the orientation and binding affinity of capping agents on NP surfaces is a technical barrier which makes it difficult to gain insight into NP synthesis. Also, quantitative evaluation like coverage density of capping agents on each crystal planes with respect to the synthesis conditions is vital information to predict the surface stability and anisotropy of the NPs. With the prior knowledge about capping agent adsorption on crystal surfaces as a function of various reaction conditions, the growth of nanoparticles along various crystal directions can be manipulated by controlling the surface coverage density as well as the binding energy of the capping agents.

The ligand-metal interaction during the NP formation can be mimicked on an electrode surface by electrosorbing ligand molecules on a charged metal surface. Detailed information about the molecular orientation can be obtained by employing various *in-situ* spectroscopic techniques such as surface enhanced Raman and surface enhanced IR spectroscopies. Moreover, knowledge about macroscopic properties of the molecule of interest is essential to bridge the knowledge gap about surface coverage and binding energy of capping agents on the metal surface. Such macroscopic information has been extracted in this thesis by making

use of the thermodynamic treatment of ideally polarizable solid electrode as well as the use of surface sensitive infrared spectroscopy.

This thesis has focused on the adsorption behaviour of MOP on Au in various chemical environments. The reasons why MOP represented an excellent choice for a case study were the following; there existed inconsistencies in the literature about the adsorption behaviour of MOP on Au surface. Moreover, DMAP, an analogous molecule of MOP had gained wide interest in nanoparticle synthesis due to its somewhat unique ability to promote NP phase transfer as well as serve as a versatile ligand. The present thesis had electrochemically evaluated MOP adsorption and shown that it behaves similar to pyridine derivatives and exhibits two states of adsorption as a function of electrode potential. Compared to DMAP, MOP adsorption on Au(111) is identical even though MOP shows weaker adsorption energy than DMAP during vertical orientation. Detailed analyses of MOP orientation on polycrystalline Au films at different electrolyte pH were achieved through SEIRAS. Moreover, the spectroscopic data agrees with the two state adsorption behaviour of MOP in both neutral and acidic electrolytes. In neutral pH, MOP adopts a vertical, N-bonded configuration at weakly charged Au surfaces, but the molecule becomes increasingly tilted at more positive potentials. Such tilting behaviour has not been reported for DMAP, and it indicates the role of the substituent on metal-pyridine interaction. Meanwhile, MOP or its conjugate acid adsorbs horizontally (π-bonded) at low pH (~4) conditions and shifts to a vertical configuration at potentials positive of the pzc for bare polycrystalline gold (~ 0.0 V).

The macroscopic (thermodynamic) and microscopic (spectroscopic) data regarding MOP adsorption of Au crystals are vital information in developing strategies to design protocols for anisotropic nanoparticles with controlled size and shape. Also, the study of MOP adsorption provides a platform to compare and contrast the adsorption behaviour of other pyridine derivatives that may open a new domain of NP stabilisers.

5.2 Future aspects

Although much has been learned about the adsorption of MOP on gold surfaces, there is still more that can be learned from a fundamental point of view. For example, it would be desirable to have surface sensitive IR measurements of MOP on Au(111) and other low-energy surfaces to compare directly with the available electrochemical data. Making Au(111) SEIRAS films without steps and terraces is challenging and alternate techniques such as Infrared Reflection Absorption Spectroscopy (IRAS) might be more suited for such studies. Additional IR studies can provide more insight into the MOP orientation, especially the tilt angle, which are not available from the current spectroelectrochemical data. Detailed information about tilting of the molecule as a function of solution pH and surface charge can be potentially useful in altering the surface coverage of MOP while designing the NP synthesis protocol. This thesis has shown that MOP and DMAP have comparable free energies of adsorption on Au(111). It remains unclear if that extends to other low index crystal planes or even polycrystalline gold. SEIRAS experiments are currently underway in the group to test the competitive adsorption of the two pyridine derivatives as a function of pH. This will provide independent assessment of the free energies of adsorption and provide new insight on how strongly the molecules compete for adsorption sites. As the work of this thesis shows that MOP and DMAP stabilize Au(111) at two different pH ranges a combination of these two surrogate ligands can stabilize NP over a wide range of pHs. The information obtained from such work might lead to good NP-synthesizing strategies that make use of multiple ligands, e.g. DMAP-stabilized seeds being introduced into MOP-containing growth solutions.

The adsorption behaviour of MOP obtained from electrochemical and spectroscopic studies provides cogent evidence to state that MOP can stabilize Au NPs. Moreover, the binding energy and surface coverage of MOP on Au (111) as a function of pH and surface potential can be effectively utilized to design protocols for NP synthesis. The affinity and density of MOP as a stabilizer on Au (111) can be manipulated by altering the solution pH and solution potential and this can, in principle, be used as a tool to modify the shape and size of the resulting nanoparticles. An extensive implementation of the results of this thesis for shape-control of gold nanoparticles is an obvious avenue for future research. Extending the results to other face-centred cubic metals would also be appealing but would require additional electrochemical and spectroelectrochemical studies of MOP's adsorption behaviour. If such approaches could be shown to be successful then it would be desirable to demonstrate the benefit of particle shape and size tuning for specific applications. For example, can new nanoparticle textures be produced for surface enhanced vibrational spectroscopies? Fine tuning of the surface enhancement at specific frequencies might be made possible with tailored MOP-stabilized NPs. Perhaps the same synthesis strategy can be employed for site specific adsorption of MOP to develop nano seeds with well-defined crystal faces to improve the NP (electro)catalytic activity.

Finally, it is important to note that the formation of anisotropic nanoparticles results from a complex set of thermodynamic and kinetic factors. Although the role of preferential adsorption by the capping agent plays an important role in determining the shape of NPs it cannot be the only the parameter to consider. The deposition rate of the metal atom onto the metal surface is an important kinetic parameter that also determines the crystal growth. In the case of Au NPs, it is evident that crystal faces of Au seeds provide a catalytic platform for the reduction of metal precursor in the presence of reducing agents and it results in the deposition of new metal atom onto the crystal surface. Surprisingly, there is no study available to

correlate the crystal structure with a rate of metal reduction/deposition, as well as the influence of adsorbed ligands on the catalytic reduction of Au. The MOP adsorption study on Au can also be extended to learn more about the effect of ligand adsorption on the rate of metal deposition.